



VGLUT3-p.A211V variant fuses stereocilia bundles and elongates synaptic ribbons

Yuvraj Joshi, Chloé P Petit, Stéphanie Miot, Marie Guillet, Gaston Sendin, Jérôme Bourien, Jing Wang, Rémy Pujol, Salah El Mestikawy, Jean-luc Puel, et al.

► To cite this version:

Yuvraj Joshi, Chloé P Petit, Stéphanie Miot, Marie Guillet, Gaston Sendin, et al.. VGLUT3-p.A211V variant fuses stereocilia bundles and elongates synaptic ribbons. *The Journal of Physiology*, In press, 599 (24), pp.5397-5416. 10.1113/JP282181 . hal-03468480

HAL Id: hal-03468480











<https://hal.sorbonne-universite.fr/hal-03468480>

Submitted on 7 Dec 2021

HAL is a multi-disciplinary open access archive for the deposit and dissemination of scientific research documents, whether they are published or not. The documents may come from teaching and research institutions in France or abroad, or from public or private research centers.

L'archive ouverte pluridisciplinaire **HAL**, est destinée au dépôt et à la diffusion de documents scientifiques de niveau recherche, publiés ou non, émanant des établissements d'enseignement et de recherche français ou étrangers, des laboratoires publics ou privés.

VGLUT3-p.A211V variant fuses stereocilia bundles and elongates synaptic ribbons

Yuvraj Joshi¹ , Chloé P. Petit¹ , Stéphanie Miot^{1,2} , Marie Guillet¹, Gaston Sendin¹ , Jérôme Bourien¹ , Jing Wang¹ , Rémy Pujol¹ , Salah El Mestikawy^{2,3} , Jean-Luc Puel¹  and Régis Nouvian^{1,4} 

¹INM, Univ Montpellier, INSERM, Montpellier, France

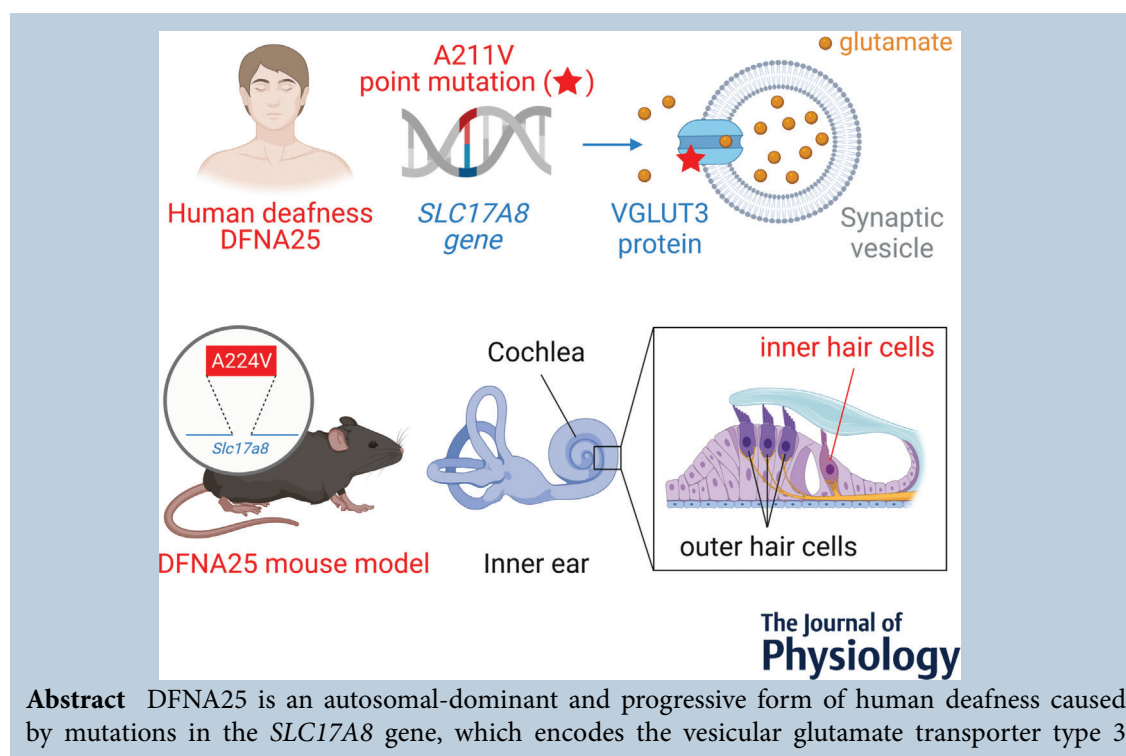
²Sorbonne Universités, Université Pierre et Marie Curie UM 119, Neurosciences Paris Seine – Institut de Biologie Paris Seine (NPS – IBPS), Paris, France

³Department of Psychiatry, Douglas Mental Health University Institute, McGill University, Montreal, Quebec, Canada

⁴INM, Univ Montpellier, INSERM, CNRS, Montpellier, France

Edited by: Ian Forsythe & Walter Marcotti

The peer review history is available in the supporting information section of this article (<https://doi.org/10.1113/JP282181#support-information-section>).



Abstract DFNA25 is an autosomal-dominant and progressive form of human deafness caused by mutations in the *SLC17A8* gene, which encodes the vesicular glutamate transporter type 3

Yuvraj Joshi earned an MPhil in biophysics from the National Institute of Mental Health and Neurosciences of Bangalore (India). Through the EU Horizon 2020 Marie Skłodowska-Curie Action Innovative Training Network, he received his PhD from the University of Montpellier at the Institute for Neurosciences of Montpellier (Hearing Research Group, <http://www.inmfrance.com>, France). His work aims to understand the mechanisms underlying auditory deficits and notably the auditory neuropathies. **Chloé P. Petit** received her MSc degree in sensory and motor neuroprostheses from the University of Montpellier (France). She is currently finishing her PhD at the same University in the Institute for Neurosciences of Montpellier (Hearing Research Group, <http://www.inmfrance.com>). Supported by the 'Fondation pour l'Audition' fellowship, she is studying the logic of sound-coding in the mammalian cochlea.



Yuvraj Joshi and Chloé P. Petit contributed equally to this work.

(VGLUT3). To resolve the mechanisms underlying DFNA25, we studied phenotypes of mice harbouring the p.A221V mutation in humans (corresponding to p.A224V in mice). Using auditory brainstem response and distortion product otoacoustic emissions, we showed progressive hearing loss with intact cochlear amplification in the VGLUT3^{A224V/A224V} mouse. The summing potential was reduced, indicating the alteration of inner hair cell (IHC) receptor potential. Scanning electron microscopy examinations demonstrated the collapse of stereocilia bundles in IHCs, leaving those from outer hair cells unaffected. In addition, IHC ribbon synapses underwent structural and functional modifications at later stages. Using super-resolution microscopy, we observed oversized synaptic ribbons and patch-clamp membrane capacitance measurements showed an increase in the rate of the sustained releasable pool exocytosis. These results suggest that DFNA25 stems from a failure in the mechano-transduction followed by a change in synaptic transfer. The VGLUT3^{A224V/A224V} mouse model opens the way to a deeper understanding and to a potential treatment for DFNA25.

(Received 20 August 2021; accepted after revision 1 November 2021; first published online 15 November 2021)

Corresponding author Régis Nouvian: Inserm U1298, Institute for Neurosciences of Montpellier, 80, rue Augustin Fliche, 34295 Montpellier Cedex 5, France. E-mail: regis.nouvian@inserm.fr

Abstract figure legend: Human deafness DFNA25 is caused by a point mutation in the *SLC17A8* gene encoding the intra-vesicular glutamate transporter type 3 (VGLUT3). In the mouse harbouring the point mutation found in humans, the inner hair cells are unable to transduce the acoustic stimulation into neural messages.

Key points

- The vesicular glutamate transporter type 3 (VGLUT3) loads glutamate into the synaptic vesicles of auditory sensory cells, the inner hair cells (IHCs).
- The VGLUT3-p.A211V variant is associated with human deafness DFNA25.
- Mutant mice carrying the VGLUT3-p.A211V variant show progressive hearing loss.
- IHCs from mutant mice harbour distorted stereociliary bundles, which detect incoming sound stimulation, followed by oversized synaptic ribbons, which release glutamate onto the afferent nerve fibres.
- These results suggest that DFNA25 stems from the failure of auditory sensory cells to faithfully transduce acoustic cues into neural messages.

Introduction

Mutations in the *SLC17A8* gene are associated with DFNA25, an autosomal-dominant and progressive form of human deafness (Ruel *et al.* 2008; Ryu *et al.* 2016). Vesicular glutamate transporters (VGLUTs) are responsible for glutamate loading into synaptic vesicles, a critical step to achieve synaptic transfer (El Mestikawy *et al.* 2011). *SLC17A8* encodes the vesicular glutamate transporter type 3 (VGLUT3; Freneau *et al.* 2002; Gras *et al.* 2002; Takamori *et al.* 2002). VGLUT3 is expressed in small subsets of neurons in the central nervous system and in the inner ear (Ruel *et al.* 2008; Seal *et al.* 2008; El Mestikawy *et al.* 2011; Zhang *et al.* 2011). In zebrafish, VGLUT3 is expressed in the ear and lateral line organ, especially in hair cells, which convert mechanical stimuli into glutamate release onto afferent fibres (Obholzer *et al.* 2008). While the loss of VGLUT3 does not alter the microphonic receptor, reflecting the

mechano-transducer current at the hair cell stereociliary bundle, it results in the absence of activity in the posterior lateral line ganglion. Accordingly, the VGLUT3 deletion abolishes the vestibulo-ocular and acoustic startle reflexes (Obholzer *et al.* 2008). In mice, the inner hair cells (IHCs), which transduce sound stimulation into glutamate secretion, express VGLUT3 (Ruel *et al.* 2008; Seal *et al.* 2008). In addition, it was recently established that outer hair cells (OHCs), which amplify acoustic input within the cochlea, also express VGLUT3 (Weisz *et al.* 2021). The genetic ablation of *SLC17A8* leads to the calcium-triggered exocytosis of empty synaptic vesicles, making the auditory afferent fibres silent (Ruel *et al.* 2008; Seal *et al.* 2008; Akil *et al.* 2012; Kim *et al.* 2019). Thus, the loss of VGLUT3 in mice results in the lack of auditory brainstem responses, reflecting a failure in the ascending auditory pathway activation. In VGLUT3-null mice, distortion product otoacoustic emissions (DPOAEs) that are a signature of the activity in OHCs are unaffected

(Ruel *et al.* 2008; Seal *et al.* 2008; Kim *et al.* 2019). In addition, it has been reported that ribbon bodies, the organelles surrounded by a monolayer of synaptic vesicles, are abnormally thin and elongated in the VGLUT3 knock-out (VGLUT3-KO or VGLUT3^{-/-}) IHC synapses (Seal *et al.* 2008; Akil *et al.* 2012). Accordingly, the ribbon volume is larger in the absence of VGLUT3 (Kim *et al.* 2019). However, the complete deafness in VGLUT3^{-/-} mice conflicts with the variable onset and progression rate of DFNA25.

The rare variant VGLUT3-p.A211V was identified as a cause of DFNA25 (Ruel *et al.* 2008). This variation does not impair the glutamate vesicular accumulation, neither the quantal release nor the quantal content in hippocampal autaptic neurons (Ramet *et al.* 2017). In addition, investigation of a mouse line harbouring the p.A221V allele in humans (p.A224V in mouse, VGLUT3^{A224V/A224V} mice) showed that this variant leads to a strong decrease of VGLUT3 expression (\approx 70%) in terminals from the central nervous system neurons without altering VGLUT3-piloted behaviour (Ramet *et al.* 2017). Thus, mechanisms depending on the VGLUT3-p.A211V variant and underlying DFNA25 auditory deficits in humans are not yet clearly understood. To tackle this point, we herein investigated the auditory system of VGLUT3^{A224V/A224V} mice. Our data show that the VGLUT3^{A224V/A224V} mice phenocopy human progressive hearing loss. In VGLUT3^{A224V/A224V} mice, the architecture of the IHC stereociliary bundle was distorted. In addition, we observed an increase of the ribbon size and a larger rate of sustained releasable pool (SRP) exocytosis. Taken together, our results reveal unexpected morphological and functional consequences of the VGLUT3-p.A224V variant that underlies DFNA25.

Material and methods

Ethical approval

Experiments were carried out in accordance with the animal welfare guidelines 2010/63/EC of the European Council Directive regarding the care and use of animals for experimental procedures and comply with the principles and regulation described in the Editorial by Grundy (2015). Animals were housed in facilities accredited by the French 'Ministère de l'Agriculture et de la Forêt' (Agreement C-34-172-36) and the experimental protocol was approved (Authorization CEEA-LR- 12111) by the Animal Ethics Committee of Languedoc-Roussillon (France).

Animals

We studied A224V mice of either sex, which have been previously described (Ramet *et al.* 2017). In

brief, the p.A211V mutation has been isolated in two unrelated human families (Ruel *et al.* 2008). In mice, the corresponding alanine is at position 224. A mouse line expressing the p.A224V mutation was generated at Phenomin – Institut Clinique de la Souris (Illkirch, France; <http://www.phenomin.fr/>) and was named VGLUT3^{A224V/A224V} as previously reported (Ramet *et al.* 2017). A point mutation was introduced in exon 5 of the mouse *SLC17A8* gene: a GCG (coding for an alanine) was exchanged for a GTG (coding for a valine). Mice were bred in-house and maintained on a C57Bl6/J genetic background. Heterozygote mice were bred to generate VGLUT3^{A224V/A224V} and wild-type littermates.

Genotyping

Genotypes of mice were determined by polymerase chain reaction (PCR) analysis of genomic DNA using FastStart PCR Master Mix (Roche Applied Science, Penzberg, Germany) as previously described (Ramet *et al.* 2017). In brief, tail or toe biopsies were digested overnight at 55°C in 300 μ l of lysis buffer (containing in mM: 100 Tris HCL pH 8.5; 5 EDTA; 0.2% SDS; 200 NaCl; pH: 8.5) with 100 μ g/ml of proteinase K (Promega, Madison, WI, USA). Samples were centrifuged for 5 min at 12,000 g and supernatants were collected. DNA was precipitated by addition of 500 μ l of isopropanol. Samples were centrifuged for 10 min at 12,000 g and supernatants were discarded. DNA was washed with 500 μ l of EtOH 70% and centrifuged for 5 min at 12,000 g. After evaporation of the EtOH, DNA was suspended in 100 μ l of water. The PCR was conducted with the following thermal cycle program: one cycle of 94°C for 8 min; 40 cycles of 94°C for 40 s, 56°C for 30 s, 72°C for 40 s; final elongation step at 72°C for 7 min. The PCR primers were the following: p1, 5'-CGGAGGGGAAGCCAGGAAAGGG-3', and p2, 5'-GACAGCTCAGTGAGCTGTAGACCCAG-3' for the wild-type and the mutated allele, yielding bands of 219 and 306 bp, respectively, which were visualized on a 2% agarose gels.

In vivo recordings

Mice were anaesthetized by an intraperitoneal injection of a mixture of Zoletil 50 (40 mg/kg) and Rompun 2% (3 mg/kg). The rectal temperature was measured with a thermistor probe and maintained at 37.1°C \pm 1°C, using a heated underblanket (Homeothermic Blanket Systems, Harvard Apparatus). Heart rate was monitored via EKG electrodes. Within 20 min of the end of the physiological session, animals were sacrificed by cervical dislocation while still under deep anaesthesia.

Auditory brainstem response and distortion product otoacoustic emission recordings

For auditory brainstem response (ABR), the acoustic stimuli consisted of 10 ms tone bursts, with a 8 ms plateau and 1 ms rise/fall time, delivered at a rate of 20.4/s with alternate polarity by a JBL 2426H loudspeaker in a calibrated free field. Stimuli were presented by varying intensities from 80 to 0 dB SPL, in 10 dB steps. Stimuli were generated and data acquired using MATLAB (MathWorks, Natick, MA, USA) and LabVIEW (National Instruments, Austin, TX, USA) software. The potential difference between vertex and mastoid intradermal needles was amplified (5000 times, VIP-20 amplifier), sampled (at a rate of 50 kHz), filtered (bandwidth of 0.3–3 kHz) and averaged (600 times). Data were displayed using LabVIEW software and stored on a computer (Dell T7400). ABR thresholds were defined as the lowest sound intensity, which elicits a clearly distinguishable response. For DPOAE recordings, an ER-10C S/N 2528 probe (Etymotic Research), consisting of two emitters and one microphone, was inserted in the left external auditory canal. Stimuli were two equilevel (65 dB SPL) primary tones of frequency f_1 and f_2 with a constant f_2/f_1 ratio of 1.2. The distortion $2f_1-f_2$ was extracted from the ear canal sound pressure and processed by the HearID auditory diagnostic system (Mimosa Acoustic) on a computer (Hewlett Packard). The probe was self-calibrated for the two stimulating tones before each recording. f_1 and f_2 were presented simultaneously, sweeping f_2 from 20 to 2 kHz in quarter octave steps. For each frequency, the distortion product $2f_1-f_2$ and the neighbouring noise amplitude levels were measured and expressed as a function of f_2 .

Electrocochleography

A retroauricular incision of the skin was performed on anaesthetized mice and the left tympanic bulla was opened. Cochlear potentials were recorded with a silver positive electrode placed on the round window membrane. The acoustic stimuli were identical to those used to elicit ABRs except for the alternate polarity. Gross cochlear potentials were amplified (2500 times, VIP-20 amplifier), sampled (at a rate of 50 kHz), filtered (bandwidth of 0.001–20 kHz), averaged (50–300 times), displayed with LabVIEW software and stored on a computer (Dell T7400). The signal was then digitally filtered using MATLAB software with a low-pass filter (cut-off frequency 3.5 kHz) to measure the compound action potential (CAP) and the summing potential (SP).

Patch-clamp recordings

After cervical dislocation of mice (1–2 months and 6 months of age), IHCs of the apical coil of freshly dissected organs of Corti were patch-clamped at their basolateral face at room temperature in tight perforated-patch configurations. The dissection solution contained the following in mM: 5.36 KCl, 141.7 NaCl, 1 $\text{MgCl}_2 \cdot 6\text{H}_2\text{O}$, 0.5 $\text{MgSO}_4 \cdot 7\text{H}_2\text{O}$, 10 Hepes and 10 D-glucose. For Ca^{2+} current and capacitance measurement recordings, the extracellular solution contained the following in mM: 2.8 KCl, 105 NaCl, 1 $\text{MgCl}_2 \cdot 6\text{H}_2\text{O}$, 2 CaCl_2 , 10 Hepes, 35 TEA-Cl, 1 CsCl, 10 D-glucose. The pipette solution for perforated patch-clamp recordings of Ca^{2+} currents contained the following in mM: 135 Cs-glutamic acid, 10 TEA-Cl, 10 4-AP, 1 $\text{MgCl}_2 \cdot 6\text{H}_2\text{O}$, 10 Hepes and 400 $\mu\text{g/ml}$ amphotericin B. Solutions were adjusted to pH 7.3 and had osmolarities between 290 and 310 mOsm/kg H_2O . All chemicals were obtained from Sigma (St. Louis, MO, USA) with the exception of amphotericin B (Calbiochem, La Jolla, USA). Patch pipettes were pulled from borosilicate glass capillaries (Kwik Fil, WPI, Worcester, MA, USA) with a two-step vertical puller PIP 6 (HEKA Elektronik, Lambrecht, Germany) and coated with silicone elastomer (Sylgard).

Ca^{2+} current recordings

Currents were low-pass filtered at 5 kHz and sampled at 10 kHz for exocytic cell membrane capacitance change (ΔC_m) and at 40 kHz for Ca^{2+} current recordings. Ca^{2+} current was isolated using P/n protocols (10 leak pulses with amplitudes of 20% of the original pulse from a holding potential of -117 mV). Cells that displayed a membrane current exceeding -50 pA at -87 mV were discarded from the analysis. No R_s compensation was applied. All voltages were corrected for liquid junction potentials calculated between pipette and bath (-17 mV). Mean resting capacitance, series and membrane resistances are indicated in Table 1.

Capacitance measurement recordings

Cell membrane capacitance (C_m) was measured using the Lindau–Neher technique (Lindau & Neher, 1988), implemented in the software-lockin module of Patchmaster (HEKA Elektronik) combined with compensation of pipette and resting cell capacitances by the EPC-10 (HEKA Elektronik) compensation circuitries. A 1 kHz, a 70 mV peak-to-peak sinusoid was applied about the holding potential of -87 mV. Given the sinewave amplitude (70 mV) and the holding potential of the hair cells ($V_m = -87$ mV), the voltage command may reach

Table 1. Biophysical properties of the inner hair cells recorded in perforated patch-clamp experiments

Age	1–2 months		6 months	
Genotype	VGLUT3 ^{+/+}	VGLUT3 ^{A224V/A224V}	VGLUT3 ^{+/+}	VGLUT3 ^{A224V/A224V}
Cm (pF)	9.5 ± 0.7	8.9 ± 0.3	7.3 ± 0.4	6 ± 0.7
Rm (GΩ)	1.5 ± 0.1	1.6 ± 0.1	1.7 ± 0.3	1.6 ± 0.3
Rs (MΩ)	29.3 ± 1.5	28.7 ± 1.1	32.3 ± 2.1	33.9 ± 2

Numbers of cells recorded: 19 and 21 IHCs from VGLUT3^{+/+} and VGLUT3^{A224V/A224V} mice at 1–2 months, respectively; 14 IHCs and 9 IHCs from VGLUT3^{+/+} and VGLUT3^{A224V/A224V} mice at 6 months, respectively.

Abbreviations: Cm, resting membrane capacitance; Rm, membrane resistance; and Rs: series resistance.

the calcium current activation threshold at the most positive excursion of the sinewave. This might lead to errors in the membrane capacitance estimates, as the membrane resistance would change. However, the 1 kHz frequency of the sinewave should minimize the calcium current contamination, as the slow kinetics of the calcium channels would prevent it from following the 1 kHz cycle-to-cycle voltage command. ΔC_m was estimated as the difference of the mean C_m over 400 ms after the end of the depolarization (the initial 250 ms was skipped) and the mean prepulse capacitance (400 ms). Mean ΔC_m estimates present grand averages calculated from the mean estimates of individual IHCs.

Immunohistochemistry, confocal and super-resolution microscopy

Immunohistochemistry was performed on whole-mount preparations of organs of Corti. Mice were decapitated after rapid cervical dislocation and their cochleas were removed from the temporal bone and dissected in phosphate buffered saline (PBS, containing in mM: 130 NaCl, 2.68 KCl, 10 Na₂HPO₄, 1.47 KH₂PO₄, pH 7.4) solution. The mid-apical cochlear turns were then fixed for 15 min in 4% paraformaldehyde diluted in PBS; afterwards, they were immuno-histochemically processed as a whole-mount. The tissues were rinsed three times for 10 min in PBS, then preincubated for 1 h in blocking solution (10% goat serum, 0.3% Triton), then incubated overnight at 4°C in the incubation solution (1% goat serum, 0.1% Triton) with primary antibodies or antisera. The primary antibodies used, and their respective dilutions were CtBP2 1:500 (BD Transduction Laboratories, San Jose, CA, USA; Cat No.:612044), Homer1 1:300 (Merck Millipore, Cat. No. ABN37) and VGLUT3 1:300 (Synaptic Systems, Cat.No. 135 204). Tissues were then rinsed three times for 10 min in wash buffer (containing in mM: 15.8 Na₂HPO₄, 2.9 NaH₂PO₄, 0.1% Triton X-100, 450 NaCl) and incubated for 2 h in the incubation solution with fluorescently labelled secondary antibodies, rhodamin-phalloidin (Molecular

probes, Eugene, OR, USA) and Hoechst dye (Invitrogen, Carlsbad, CA, USA). They were finally rinsed four times for 10 min in wash buffer and mounted in Dako fluorescence mounting medium (code-s3023, Agilent Technologies, Inc. Santa Clara, CA, USA). Tissues were examined with the Zeiss LSM880 (Zeiss, Oberkochen, Germany) airyscan or confocal microscopes of the Montpellier Resource Imaging facility (Montpellier, France). Image stacks were then processed with ImageJ software (Wayne Rasband, National Institutes of Health, USA). The quantifications of ribbons and synapses, that is, juxtaposed spots of the pre-synaptic ribbon component RIBEYE and post-synaptic density protein Homer, were performed in Z-stack confocal images using a 3D custom algorithm (Bourien *et al.* 2014). Mean ribbon and synapse estimates present grand averages calculated from the mean estimates of individual cochleas.

For stimulated emission depletion (STED) microscopy imaging, secondary goat anti-guinea pig Alexa-488 1:1000 (Cat.-Nr. A11039; Thermo Fisher Scientific), goat anti-mouse IgG, Abberior STAR RED 1:200 (STRED-1001-500UG, Abberior GmbH) and goat anti-rabbit IgG, Abberior STAR-580 1:200 (ST580-1002-500UG, Abberior GmbH) antibodies were applied for 2 h at room temperature. After mounting the specimen in Dako mounting medium, image acquisition was performed using an Abberior Instruments Expert Line STED microscope (Abberior Instruments GmbH; based on an Olympus IX83 inverted microscope) in confocal and/or STED mode using a 1.4 NA UPlanSApo 100x oil immersion objective lens. We employed two pulsed lasers 580 nm (red) and 647 nm (far-red) for excitation and a pulsed 775 nm laser for STED. Image stacks were acquired with Inspector Software, keeping xy pixel sizes of 30 × 30 nm and step sizes of 50 nm (3D-STED). xy pixel sizes in 2D-STED were kept at 30 × 30 nm. The microscope is housed at the Montpellier Resource Imaging (MRI) facility (Montpellier, France). Image stacks were then processed using ImageJ (FiJi) software (Wayne Rasband, National Institutes of Health, USA) and ribbon size analysis was achieved by using custom written script in the MATLAB software over

Table 2. Numbers of mice, cochleae and hair cells examined in scanning electron microscopy in VGLUT3^{+/+}, VGLUT3^{+/-} and VGLUT3^{A224V/A224V} mice at 1, 2, 4 and 6 months of age

Age	1 month	2 months	4 months	6 months
VGLUT3 ^{+/+}	Three mice Three cochleae IHCs: 815 OHCs: 2931	Two mice Two cochleae IHCs: 472 OHCs: 1860	Six mice Six cochleae IHCs: 1366 OHCs: 5121	Four mice Four cochleae IHCs: 973 OHCs: 3341
VGLUT3 ^{+/-} A224V	Two mice Three cochleae IHCs: 743 OHCs: 3171	Three mice Three cochleae IHCs: 1140 OHCs: 4580	Two mice Two cochleae IHCs: 552 OHCs: 2175	Two mice Two cochleae IHCs: 1115 OHCs: 3948
VGLUT3 ^{A224V/A224V}	Five mice Six cochleae IHCs: 1217 OHCs: 5256	Two mice Three cochleae IHCs: 732 OHCs: 3015	Four mice Four cochleae IHCs: 1140 OHCs: 4459	Four mice Four cochleae IHCs: 765 OHCs: 2654

IHC: inner hair cell; OHC: outer hair cell.

30 IHCs ($n = 4$ cochleas) at 2 months, 73 IHCs ($n = 4$ cochleas) at 4 months, 61 IHCs ($n = 4$ cochleas) at 6 months from VGLUT3^{+/+} mice and 39 IHCs ($n = 3$ cochleas) at 2 months, 118 IHCs ($n = 3$ cochleas) at 4 months, 83 IHCs ($n = 4$ cochleas) at 6 months from VGLUT3^{A224V/A224V} mice. Measurement of ribbon size was obtained by (i) surrounding the ribbon using *contour* function (iso-intensity line fixed at mean background + 2 SD) and (ii) quantifying length of long axis (a_{lg}) and short axis (a_{sh}) using the *fit_ellipse* function (least-squares criterion). The elliptical surface (S_{el}) was then calculated using the equation $S_{el} = (a_{lg} \times a_{sh} \times \pi)/4$.

Electron microscopy

Scanning (SEM) and transmission (TEM) electron microscopy were done for the anatomical examination of cochlear hair cells. For both techniques, the animals were decapitated under deep anaesthesia (pentobarbital, 50 mg/kg), their cochleas were removed from the temporal bone. For SEM, PBS-washed cochleae were fixed with 2.5% glutaraldehyde in phosphate buffer, pH 7.2 for 2 h at room temperature, followed by washing in phosphate buffer. The bony capsule of the cochlea was dissected out, and the stria vascularis as well as the tectorial and Reissner's membranes were removed. Fixed cochleae were dehydrated using a graded ethanol series (15–100%), followed by critical point drying with CO₂. Subsequently, the samples were sputter-coated with an approximatively 10 nm thick gold film and then examined under a scanning electron microscope (Hitachi S4000) using a lens detector with an acceleration voltage of 10 kV at calibrated magnifications. The numbers of mice, cochleae and total numbers of IHCs and OHCs are given in the Table 2.

For TEM, the cochleae were perfused with a solution of 2.5% glutaraldehyde in PHEM buffer (1X, pH 7.4) and immersed in the same fixative for 1 h at room temperature, then overnight at 4°C. Samples were then rinsed in PHEM buffer and post-fixed in a 0.5% osmic acid for 2 h in the dark and at room temperature. After two rinses in PHEM buffer, the cells were dehydrated in a graded series of ethanol solutions (30–100%). The cells were embedded in EmBed 812 using an Automated Microwave Tissue Processor for Electronic Microscopy, Leica EM AMW. Thin sections (70 nm; Leica-Reichert Ultracut E) were collected at different levels of each block. These sections were counterstained with uranyl acetate 1.5% in 70% ethanol and lead citrate and observed using a Tecnai F20 transmission electron microscope at 200 KV. Both SEM and TEM were carried out at the CoMET facility (MRI, INM, Montpellier, France).

Data analysis

Data were analysed using Igor Pro (WaveMetrics, Lake Oswego, OR, USA), MATLAB and R (R core team) software. All these data are expressed as means \pm standard deviation (SD) and were compared by two-tailed Mann–Whitney Wilcoxon's test, Student's *t* test or a two-sample test for equality of proportions.

Results

Auditory neuropathy in VGLUT3^{A224V/A224V} mouse

We first examined the synchronous activation of the ascending auditory system of wild-type (VGLUT3^{+/+}) mice, heterozygous (VGLUT3^{+/-}A224V) mice and homozygous (VGLUT3^{A224V/A224V}) mice (Fig. 1). In heterozygous mice, we observed a slight threshold shift

(mean threshold at 1 month: 28.2 ± 5.81 dB SPL vs. 33.6 ± 1.88 dB SPL in VGLUT3^{+/+} and VGLUT3^{+/A224V} mice, respectively, $P = 0.003$, two-tailed Mann–Whitney Wilcoxon's test; at 6 months: 43.4 ± 6.1 dB SPL vs. 53 ± 3.8 dB SPL in VGLUT3^{+/+} and VGLUT3^{+/A224V} mice, respectively, $P = 0.001$, two-tailed t test; Fig. 1*F–J*). However, the reduction of ABRs did not reach a significant difference in comparison with wild-type littermates (Fig. 1*A–E*). In contrast, VGLUT3^{A224V/A224V} mice showed a decrease in the ABR amplitude from 1 up to 6 months of age (mean wave 1 ABR amplitude at 1 month: 2.4 ± 0.6 μ V vs. 1.7 ± 0.3 μ V in VGLUT3^{+/+} mice and VGLUT3^{A224V/A224V} mice, respectively, $P = 0.001$; at 6 months: 0.85 ± 0.3 μ V vs. 0.23 ± 0.2 μ V in VGLUT3^{+/+} and VGLUT3^{A224V/A224V} mice, respectively, $P = 0.0003$, two-tailed Mann–Whitney Wilcoxon's test; Fig. 1*A–E*). The alteration in the ABR waveform was associated with a progressive threshold shift (mean threshold at 1 month: 28.2 ± 5.8 dB SPL vs. 35.4 ± 10.2 dB SPL in VGLUT3^{+/+} and VGLUT3^{A224V/A224V} mice, respectively, $P = 0.007$; at 6 months: 43.4 ± 6.1 dB SPL vs.

67.7 ± 6 dB SPL in VGLUT3^{+/+} and VGLUT3^{A224V/A224V} mice, respectively, $P = 1.10^{-6}$, two-tailed Mann–Whitney Wilcoxon's test; Fig. 1*F–J*). To determine whether the hearing loss was due to defective OHCs, we probed the DPOAEs. We observed robust DPOAEs in the heterozygote and homozygote mice, indicating that OHC mechanical activity was essentially preserved ($2f_1$ – f_2 @ f_2 11.9 kHz: 39.6 ± 7.3 dB SPL, 38.5 ± 4.3 dB SPL and 44.4 ± 7.6 dB SPL in 6-month-old VGLUT3^{+/+} mice, VGLUT3^{+/A224V} mice and VGLUT3^{A224V/A224V} mice, respectively; Fig. 1*K–O*). Altogether, VGLUT3^{A224V/A224V} mice showed a progressive hearing loss with functional cochlear amplification.

Next, we carried out electrocochleography to probe the activity of IHCs and the synchronous activation of afferent fibres (Fig. 2*A*). CAP was strongly diminished in 1- to 2-month-old VGLUT3^{A224V/A224V} mice, consistent with the reduction of the ABR wave 1 (mean CAP N_1 – P_1 amplitude: 203.4 ± 80.6 μ V vs. 80.7 ± 37 μ V in VGLUT3^{+/+} and VGLUT3^{A224V/A224V} mice, respectively, $P = 1.10^{-6}$, two-tailed Mann–Whitney Wilcoxon's test;

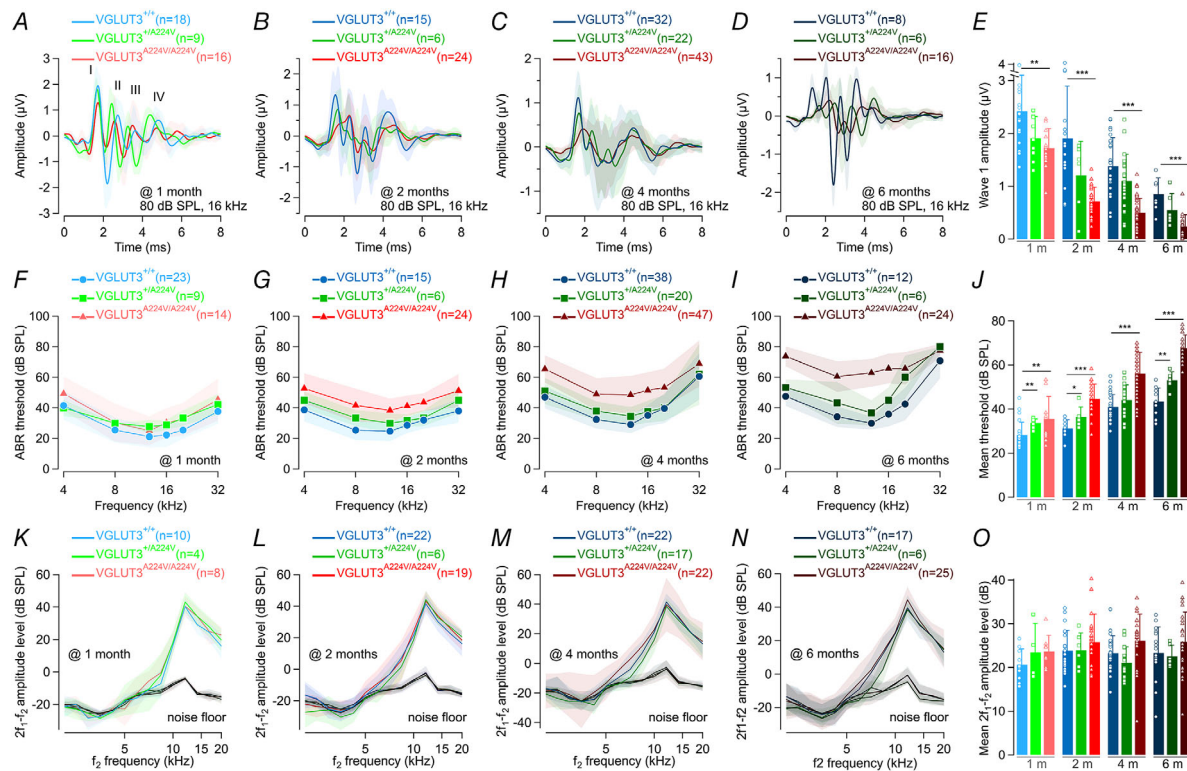


Figure 1. Progressive hearing loss in the VGLUT3^{A224V/A224V} mouse line

A–D, mean auditory brainstem response (ABR) \pm SD recordings evoked by 16 kHz tone burst at 80 dB SPL from 1–6-month-old VGLUT3^{+/+}, VGLUT3^{+/A224V} and VGLUT3^{A224V/A224V} mice. *E*, mean wave 1 ABR \pm SD amplitude from (*A–D*). *F–J*, mean ABR \pm SD audiograms from 1–6-month-old VGLUT3^{+/+}, VGLUT3^{+/A224V} and VGLUT3^{A224V/A224V} mice. *J*, mean threshold \pm SD from (*F–I*). *K–N*, DPOAEs from 1–6-month-old VGLUT3^{+/+}, VGLUT3^{+/A224V} and VGLUT3^{A224V/A224V} mice. The $2f_1$ – f_2 amplitude level is shown as a function of f_2 frequency. The black lines indicate the background noise level. *O*, mean $2f_1$ – f_2 \pm SD amplitude level from (*K–N*) measured between 5 and 20 KHz. *n* indicates the number of cochleae recorded. Level of significance: * $P < 0.05$; ** $P < 0.01$; *** $P < 0.001$, two-tailed Mann–Whitney Wilcoxon's test, Student's t test. Symbols represent individual cochleae.

Fig. 2B). In addition, we observed a smaller SP, reflecting the receptor potential in IHCs (mean SP amplitude: $93.3 \pm 57.1 \mu\text{V}$ vs. $50.2 \pm 50.8 \mu\text{V}$ in $\text{VGLUT3}^{+/+}$ and $\text{VGLUT3}^{\text{A224V/A224V}}$ mice, respectively, $P = 0.007$, two-tailed Mann–Whitney Wilcoxon's test; Fig. 2C). These results implied a selective alteration of the IHC's function in $\text{VGLUT3}^{\text{A224V/A224V}}$ homozygous mice.

Alteration at the stereociliary bundle in $\text{VGLUT3}^{\text{A224V/A224V}}$ mouse inner hair cells

Given the reduction in the SP, we examined the ultrastructure of the stereocilia bundle from IHCs at the mid-apical region of the cochlea (e.g. the region encoding frequency up to 20 kHz) using SEM (Fig. 3). In $\text{VGLUT3}^{+/+}$ mice, the apical side of IHCs projected distinct and erected stereocilia (Figs. 3A–D and 4A–D). In heterozygous mice, stereocilia bundles were found to be normal at 1 month of age (Figs. 3E and 4E, M) but a small fraction of IHCs harbouring fused stereocilia was observed at 2 months ($2.7 \pm 0.7\%$ vs. $8.6 \pm 0.8\%$ in $\text{VGLUT3}^{+/+}$ and $\text{VGLUT3}^{\text{A224V/A224V}}$ mice, respectively, $P = 4.10^{-5}$, two-sample test for equality of proportions; Figs. 3F and 4F, N). Although some IHCs with a distorted bundle were seen, the number of IHCs with these abnormal stereocilia did not differ between heterozygous and wild-type mice at later ages (Figs. 3G–H and 4G–H, O–P). In homozygous $\text{VGLUT3}^{\text{A224V/A224V}}$ mice, we found more than 20% IHCs with splayed stereocilia already at 1 month ($4.8 \pm 0.7\%$ vs. $23.7 \pm 1.2\%$ in $\text{VGLUT3}^{+/+}$ mice and $\text{VGLUT3}^{\text{A224V/A224V}}$ mice, respectively, $P = 2.10^{-16}$, two-sample test for equality of proportions; Figs. 3I and 4I, M). Collapsed

bundles were frequently observed at later stages ($9.5 \pm 0.8\%$ vs. $35.1 \pm 1.4\%$ in 4-month-old $\text{VGLUT3}^{+/+}$ and $\text{VGLUT3}^{\text{A224V/A224V}}$ mice, respectively, $P = 2.10^{-16}$, two-sample test for equality of proportions; Figs. 3J–L and 4J–L, N–P). By plotting the percentage of normal, altered and missing hair cells as a function of the age, we found that the fraction of IHCs with massive fusion or even absent cilia apparatus significantly increased with age ($12.7 \pm 1\%$ vs. $61 \pm 1.7\%$ in 6-month-old $\text{VGLUT3}^{+/+}$ and $\text{VGLUT3}^{\text{A224V/A224V}}$ mice, respectively, $P = 2.10^{-16}$, two-sample test for equality of proportions; Fig. 6A). Together, these data suggest that the threshold shift in $\text{VGLUT3}^{\text{A224V/A224V}}$ mice is associated with a defective ultrastructure of stereocilia from IHCs.

OHCs had a normal appearance, even though the IHCs with disrupted bundles were located at the same region (Figs. 3 and 6B). High magnification SEM micrograph confirmed that the stereocilia bundle in OHCs appeared well-organized, with a staircase pattern, consistent with preserved DPOAEs (Fig. 5). Altogether, these data indicated a selective alteration of the stereocilia from IHCs.

VGLUT3 is normally distributed in inner hair cells from $\text{VGLUT3}^{\text{A224V/A224V}}$ mice

The variant strongly decreases (~70%) the expression of VGLUT3-p.A224V in the terminals of the striatum or hippocampus neurons, leaving its accumulation in the soma unaffected (Ramet *et al.* 2017). Thus, we wondered whether the p.A224V variant might alter the distribution of VGLUT3 within IHCs, especially in the basolateral area. Semi-quantitative analysis of the VGLUT3

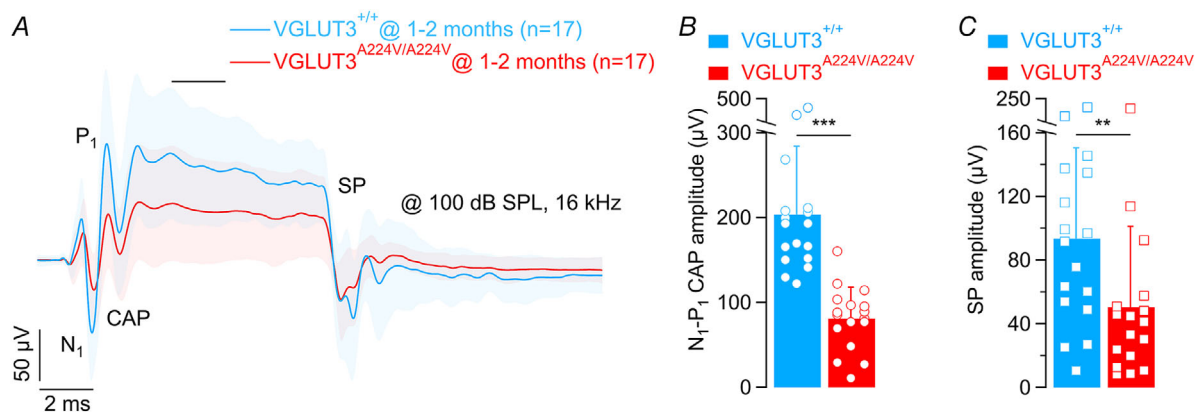


Figure 2. Inner hair cell receptor potential is altered in $\text{VGLUT3}^{\text{A224V/A224V}}$ mouse

A, mean compound action potential (CAP; N₁–P₁ amplitude) ± SD and summing potential (SP) ± SD, reflecting the auditory afferent fibre activation and inner hair cell receptor potential, respectively. CAP and SP were evoked by 16 kHz tone burst at 100 dB SPL in 1–2-month-old $\text{VGLUT3}^{+/+}$ and $\text{VGLUT3}^{\text{A224V/A224V}}$ mice. *n* indicates the number of cochleae recorded. B and C, mean CAP amplitude ± SD (B) and SP amplitude ± SD (C) from 1–2-month-old $\text{VGLUT3}^{+/+}$ and $\text{VGLUT3}^{\text{A224V/A224V}}$ mice. SP were measured at the black marker in (A). Level of significance: ** $P < 0.01$; *** $P < 0.001$, two-tailed Mann–Whitney Wilcoxon's test. Symbols represent individual cochleae.

immunofluorescence throughout the cell, from the upper side of the nucleus to the basolateral side, showed similar targeting of VGLUT3-p.A224V between both genotypes (VGLUT3 immunofluorescence: 1710 ± 219 A.U. vs. 1678 ± 416 A.U. $\times \mu\text{m}$ in IHCs from 4-month-old VGLUT3^{+/+} and VGLUT3^{A224V/A224V} mice, respectively, $P = 0.565$; Fig. 7). Therefore, in contrast to what is observed in the central nervous system neurons (Ramet *et al.* 2017), the p.A224V variant does not disturb the VGLUT3 targeting within the hair cell cytoplasm.

Alteration of the synaptic ribbon size in VGLUT3^{A224V/A224V} mouse inner hair cells

Given the role of VGLUT3 in the synaptic transfer between the IHC and the afferent nerve fibre, we addressed the question of whether additional consequences might occur in the pre-synaptic compartment and specifically in the synaptic ribbon. Figure 8 shows transmission electron microscopy examples of plasma-membrane anchored synaptic ribbons with a halo of synaptic vesicles. Multiple ribbons facing a single afferent terminal were observed in the IHCs from VGLUT3^{A224V/A224V} mice but the low number of samples in our study precluded any quantitative analysis. Indeed, multiple ribbons are also found in a fraction of synapses in adults (Merchan-Perez & Liberman, 1996; Michanski *et al.* 2019; Payne *et al.* 2021). Therefore, we used immunolabelling to measure the number

and size of synaptic ribbons. From 2 to 6 months, the number of ribbons immunolabelled with anti-Ctbp2 antiserum was comparable between wild-type mice and VGLUT3^{A224V/A224V} mice (Fig. 9A–E). In addition, we did not notice any difference in the ribbon synapse number corresponding to the juxtaposed immunostainings of Ctbp2 and post-synaptic scaffolding protein Homer (at 6 months: 10.5 ± 1.9 synapses per IHC vs. 11 ± 0.7 synapses per IHC in VGLUT3^{+/+} mice and in VGLUT3^{A224V/A224V} mice, respectively, $P = 0.642$; Fig. 9F). However, synaptic ribbons became abnormally elongated in knock-in mice (Fig. 9B, D). Using STED super-resolution microscopy in 2-month-old mice, Ctbp2-immunolabelled signals looked like ovoid spots. Synaptic ribbons in VGLUT3^{A224V/A224V} mice were slightly but significantly larger (long object axis: 440.3 ± 125 nm vs. 458.2 ± 114 nm in VGLUT3^{+/+} mice and VGLUT3^{A224V/A224V} mice, respectively, $P = 0.213$; short object axis: 287.4 ± 48 nm in VGLUT3^{+/+} and 302.4 ± 50 nm VGLUT3^{A224V/A224V} mice, respectively, $P = 0.009$, Student's *t* test; Fig. 10A–C). In contrast, we could quantify a drastic elongation of ribbons from IHCs in VGLUT3^{A224V/A224V} mice at 4 and 6 months (at 6 months: long object axis: 473.7 ± 142 nm vs. 602.2 ± 285 nm in VGLUT3^{+/+} and VGLUT3^{A224V/A224V} mice, respectively, $P = 2.10^{-20}$; short object axis: 300.1 ± 61 nm in VGLUT3^{+/+} and 344.4 ± 111 nm VGLUT3^{A224V/A224V} mice, respectively, $P = 1.10^{-15}$, Student's *t* test; Fig. 10D–I). Consistently, mean elliptical size calculated from long and short ribbon axes were comparable at 2 months of age between the genotypes but significantly increased at

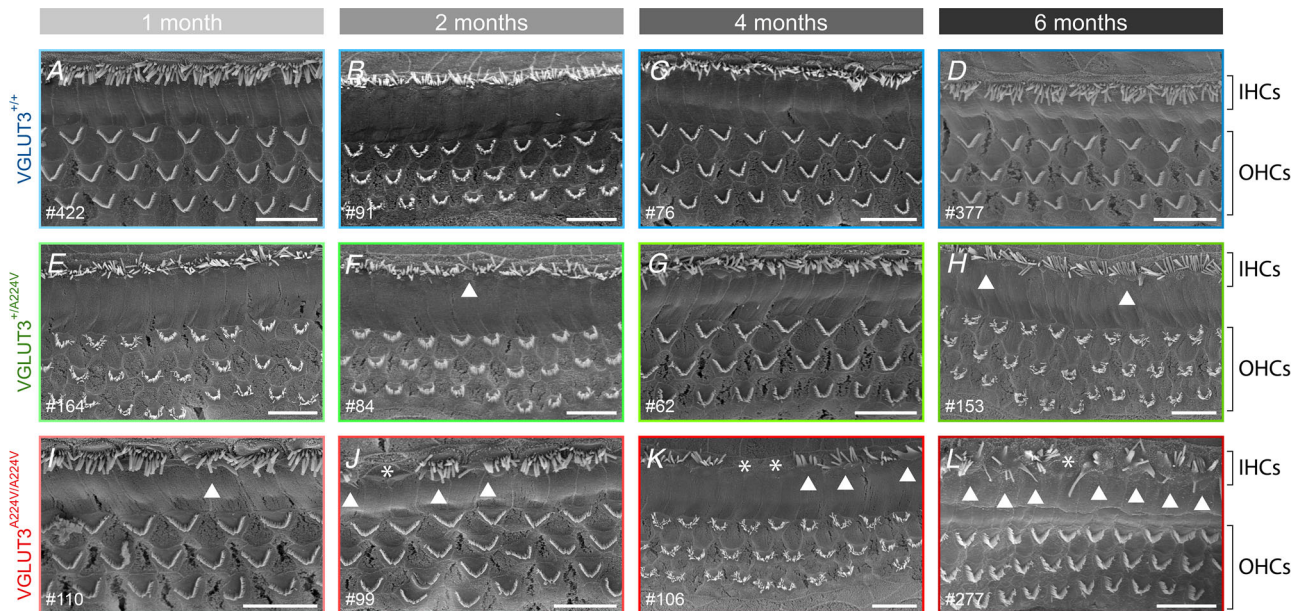


Figure 3. Ultrastructure of the cochlear sensory epithelium

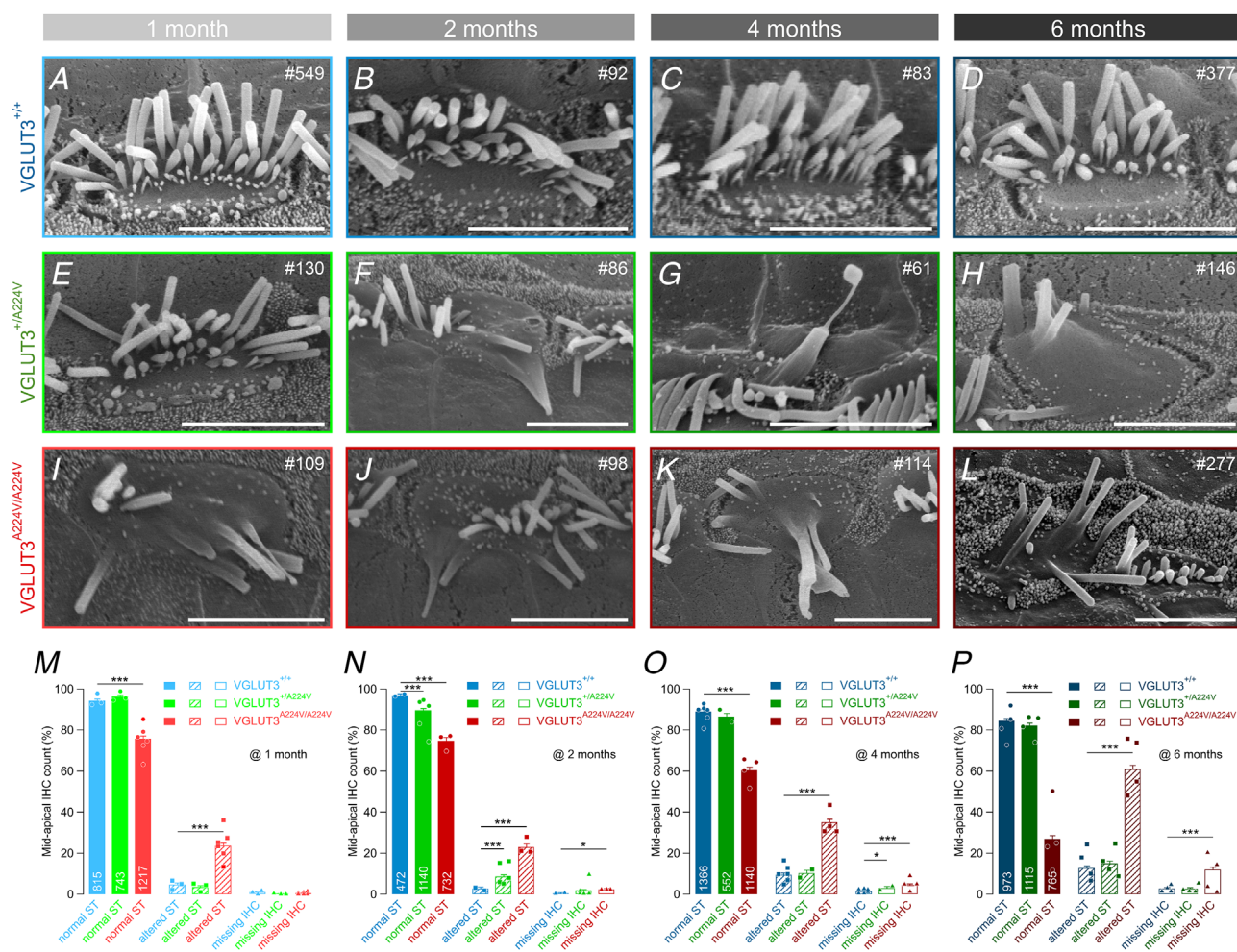
A–L, SEM of the organ of Corti from mid-apical turns in 1–6-month-old VGLUT3^{+/+}, VGLUT3^{+/A224V} and VGLUT3^{A224V/A224V} mice. # Indicates the animal's number. IHCs: inner hair cells; OHCs: outer hair cells. Arrow and star indicate fused stereocilia and missing hair cells, respectively. Scale bars: 10 μm .

4 and 6 months in IHCs from $VGLUT3^{A224V/A224V}$ mice (elliptical size: $0.102 \pm 0.04 \mu\text{m}^2$ vs. $0.111 \pm 0.04 \mu\text{m}^2$ in 2-month-old $VGLUT3^{+/+}$ and $VGLUT3^{A224V/A224V}$ mice, respectively and $0.116 \pm 0.05 \mu\text{m}^2$ vs. $0.18 \pm 0.15 \mu\text{m}^2$ in 6-month-old $VGLUT3^{+/+}$ and $VGLUT3^{A224V/A224V}$ mice, respectively, $P = 3.10^{-4}$, Student's t test; Fig. 11A). Size distributions were skewed for 4- and 6-month-old $VGLUT3^{A224V/A224V}$ mice (Fig. 11B). The cumulative size histogram showed that IHCs from 6-month-old $VGLUT3^{A224V/A224V}$ mice contain ribbons resembling those found at 2 months as well as ribbons for which size increased up to 100 % (ribbon size up to $0.064 \mu\text{m}^2$ and $0.065 \mu\text{m}^2$ within the 10th percentile against $0.17 \mu\text{m}^2$ and $0.35 \mu\text{m}^2$ within the 90th percentile from 6 month IHCs in $VGLUT3^{+/+}$ mice and $VGLUT3^{A224V/A224V}$ mice, respectively; Fig. 11C). These results indicated that the p.A224V variant did not affect ribbons in

the same manner. Small synaptic bodies remained small, while large pre-synaptic ribbons became larger in $VGLUT3^{A224V/A224V}$ mice.

Calcium-triggered exocytosis in $VGLUT3^{A224V/A224V}$ mouse inner hair cells

To determine whether synaptic release was affected in IHCs of $VGLUT3^{A224V/A224V}$ mice, we measured the membrane capacitance as a proxy of calcium-triggered exocytosis using perforated patch-clamp (Fig. 12). In hair cells, voltage steps of short duration (under 20 ms) recruit the readily releasable pool (RRP) that corresponds to the release of synaptic vesicles in the vicinity of the calcium channels, while longer duration of the stimuli (beyond 20 ms) mobilizes the SRP which reflects the exocytosis of remote vesicles and/or the resupply of synaptic vesicles



to the release site (Moser & Beutner, 2000). In our experiments, secretion by IHCs was tested at two different time points: that is, before (1–2 months of age) and after (6 months) the elongation of synaptic ribbons. As shown in Fig. 12A, depolarizing voltage steps evoked calcium influx, which in turn triggered the fusion of synaptic vesicles to the plasma membrane, mirrored by jumps in the membrane capacitance. Between 1 and 2 months, the calcium current–voltage relationships were comparable (calcium peak current I_{Ca} : -155.2 ± 34.9 pA vs. -159.1 ± 35.2 pA for VGLUT3^{+/+} mice and VGLUT3^{A224V/A224V}, respectively, $P = 0.817$; Fig. 12B1). Furthermore, the exocytic membrane capacitance was of indistinguishable amplitude between genotypes for any stimulus duration (ΔC_{m20ms} 12.6 ± 5.8 fF vs. 14.6 ± 6.9 fF for VGLUT3^{+/+} mice and VGLUT3^{A224V/A224V} mice, respectively, $P = 0.297$; ΔC_{m100ms} 38.9 ± 14.6 fF vs. 35.3 ± 12.7 fF for

VGLUT3^{+/+} and VGLUT3^{A224V/A224V}, respectively, $P = 0.489$; Fig. 12C1). In addition, the calcium influx was of similar amplitude ($Q_{Ca^{2+}20ms}$ 2.9 ± 0.6 pC vs. 3 ± 0.6 pC for VGLUT3^{+/+} mice and VGLUT3^{A224V/A224V} mice, respectively, $P = 0.578$; $Q_{Ca^{2+}100ms}$ 13.8 ± 3.1 pC vs. 14.3 ± 3.2 pC for VGLUT3^{+/+} mice and VGLUT3^{A224V/A224V} mice, respectively, $P = 0.456$; Fig. 12C1). Thus, the exocytosis jumps plotted against the corresponding calcium influx overlapped (Fig. 12D1) and the release efficiency, that is, the exocytosis per unit of incoming calcium, was not different between wild-type mice and homozygous mice for short and long depolarizing voltage steps ($\Delta C_m/Q_{Ca^{2+}20ms}$: 4.4 ± 2.3 fF/pC vs. 4.8 ± 2 fF/pC, $P = 0.309$ and $\Delta C_m/Q_{Ca^{2+}100ms}$: 2.8 ± 0.8 fF/pC vs. 2.5 ± 0.7 fF/pC, $P = 0.249$ for VGLUT3^{+/+} mice and VGLUT3^{A224V/A224V} mice, respectively; Fig. 12E1). At 6

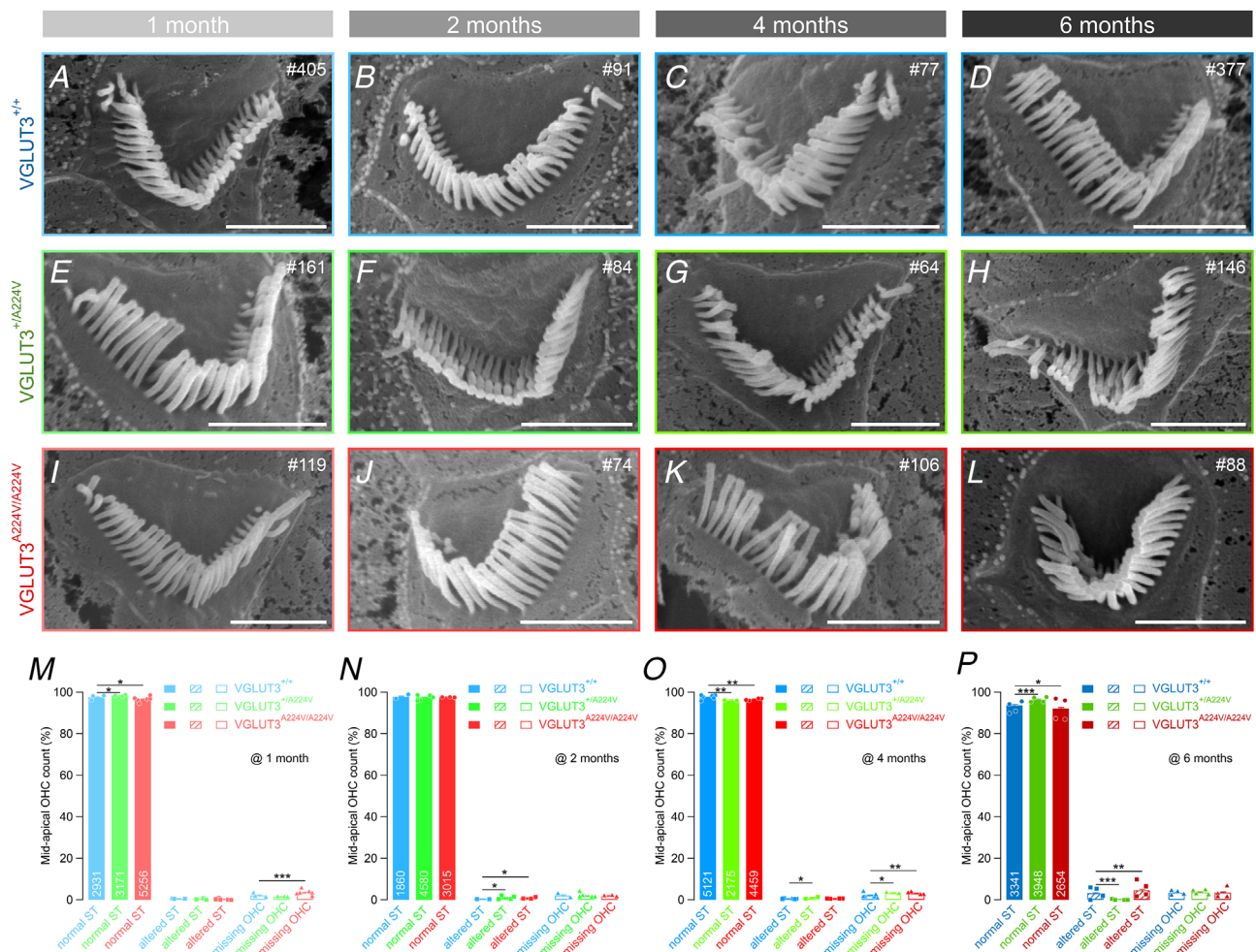


Figure 5. Stereociliary bundle morphology in outer hair cells

A–L, SEM of the stereocilia bundle from outer hair cells (OHCs) at mid-apical turns in 1–6-month-old VGLUT3^{+/+}, VGLUT3^{+/A224V} and VGLUT3^{A224V/A224V} mice. Scale bars: 2 μ M. M–P, fraction of OHCs harbouring normal or altered stereocilia (ST) and of missing OHCs. # Indicates the animal's number. Percentages are shown with their SD. Total numbers of OHCs examined are indicated in the histograms. Symbols represent individual cochleae. Level of significance: * $P < 0.05$; ** $P < 0.01$; *** $P < 0.001$, two-sample test for equality of proportions.

months of age, the calcium current–voltage relationship still did not substantially differ between genotypes (calcium peak current I_{Ca} : -127.9 ± 23 pA vs. -147.7 ± 49.5 pA for VGLUT3^{+/+} mice and VGLUT3^{A224V/A224V} mice, respectively, $P = 0.231$; Fig. 12B2). Although the exocytosis in IHCs evoked by short time stimulus duration (RRP, under 20 ms) remained identical (ΔC_{m20ms}

8.7 ± 5.5 fF vs. 11.9 ± 6.6 fF for VGLUT3^{+/+} mice and VGLUT3^{A224V/A224V} mice, respectively, $P = 0.270$; Fig. 12C2), we observed a larger increase of exocytosis from IHC VGLUT3^{A224V/A224V} mice in response to long depolarizing voltage steps (ΔC_{m100ms} : 32.7 ± 17.8 fF vs. 55.6 ± 25.1 fF for VGLUT3^{+/+} and VGLUT3^{A224V/A224V}, respectively; $P = 0.025$, two-tailed Mann–Whitney

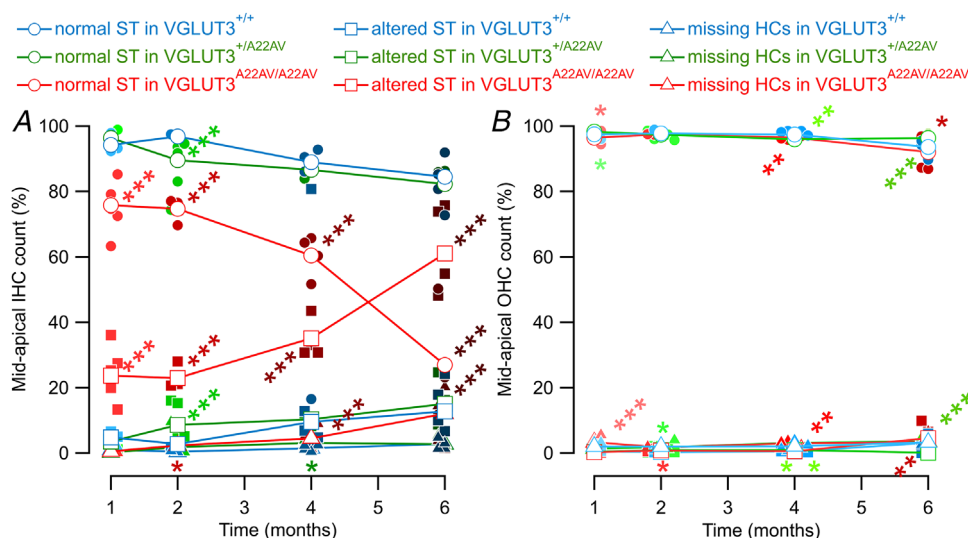


Figure 6. Time course of the stereocilia bundle alteration

Percentage of normal (empty circle), altered (filled square) and missing (empty triangle) IHC (A) and outer hair cell (B) plots as a function of the age in the VGLUT3^{+/+} (blue), VGLUT3^{+/A224V} (green) and VGLUT3^{A224V/A224V} (red) mice. Percentages are shown with their confidence interval. Stars indicate significant difference between heterozygotes (green star) or homozygotes (red star) vs. wild type. Symbols represent individual cochleae. Level of significance: * $P < 0.05$; ** $P < 0.01$; *** $P < 0.001$, two-sample test for equality of proportions.

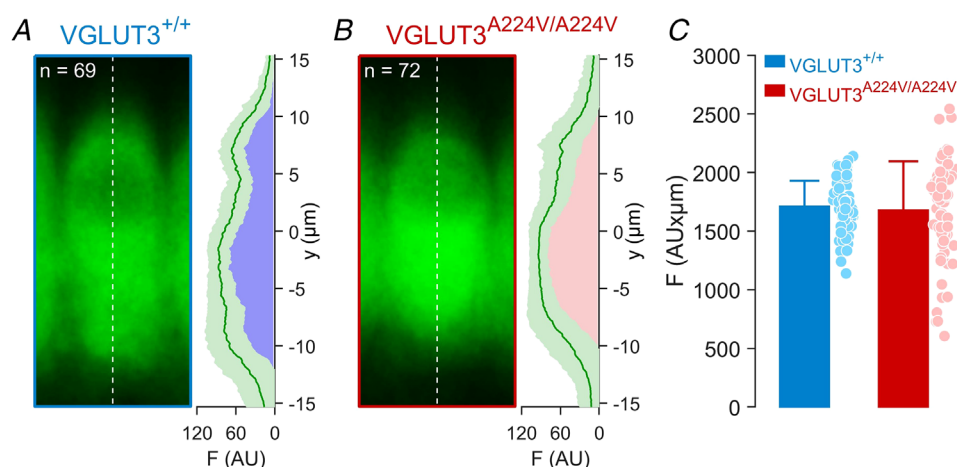


Figure 7. VGLUT3 distribution in inner hair cells from VGLUT3^{+/+} and VGLUT3^{A224V/A224V} mice

A and B, maximum projection average of confocal sections of 4-month-old VGLUT3^{+/+} (A) and VGLUT3^{A224V/A224V} (B) mid-apical turns IHCs immunolabelled against VGLUT3 (green) processed and imaged under identical conditions. Left panel: IHCs have been centred in respect to the centroid of the nucleus; right panel: average of the maximum projection fluorescence \pm SD measured through the vertical central axis crossing the IHCs (dashed white line). n indicates the number of IHCs immunolabelled from four cochleae for each genotype. C, semi-quantitative analysis of VGLUT3 immunofluorescence. Bar histograms represent the integral of the maximum projection fluorescence \pm SD measured through the vertical central axis crossing the IHCs of 4-month-old VGLUT3^{+/+} (blue) and VGLUT3^{A224V/A224V} (red) corresponding to (A and B), respectively. Symbols represent individual hair cells.

Wilcoxon's test; Fig. 12C2). Consequently, the rate of the sustained exocytosis measured by the slope of the line fit to the exocytic capacitance between 20 and 100 ms increased in homozygous mice ($\Delta C_{m20-100ms}$ $300.1 \pm 174 \text{ fF.s}^{-1}$ vs. $545.4 \pm 278.5 \text{ fF.s}^{-1}$ for VGLUT3^{+/+} mice and VGLUT3^{A224V/A224V} mice, respectively; $P = 0.021$, two-tailed Mann–Whitney Wilcoxon's test). To determine whether the larger secretion was due to an increase in the corresponding calcium influx, we first measured the calcium influx but we did not find a significant difference between the mouse lines ($Q_{Ca^{2+}}^{100ms}$ $11.2 \pm 2.5 \text{ pC}$ vs. $13.6 \pm 5.1 \text{ pC}$ for VGLUT3^{+/+} mice and VGLUT3^{A224V/A224V} mice, respectively, $P = 0.425$; Fig. 12C2). Next, we plotted the membrane capacitance changes against the corresponding calcium entry. Still, we found an increase in release for overlapping range of incoming calcium (Fig. 12D2). Finally, the release efficiency was comparable between wild-type mice and homozygous mice for short depolarizing steps ($C_m/Q_{Ca^{2+}}^{20ms}$: $3.5 \pm 2.1 \text{ fF/pC}$ vs. $4.2 \pm 1.8 \text{ fF/pC}$ for VGLUT3^{+/+} mice and VGLUT3^{A224V/A224V} mice, respectively, $P = 0.242$; Fig. 12E2) but larger in the VGLUT3^{A224V/A224V} homozygous mice for longer duration ($C_m/Q_{Ca^{2+}}^{100ms}$: $2.8 \pm 1.4 \text{ fF/pC}$ and $4.3 \pm 1.7 \text{ fF/pC}$ for VGLUT3^{+/+} mice and VGLUT3^{A224V/A224V} mice, respectively; $P = 0.036$, two-tailed Mann–Whitney Wilcoxon's test; Fig. 12E2). Thus, the p.A224V variant of

the *SLC17A8* gene is associated with an increase in the SRP leaving the calcium influx unaffected.

Discussion

In this study, we showed that the mutant mouse carrying the p.A224V variant of the *SLC17A8* gene develops a progressive hearing loss, phenocopying human auditory neuropathy. The mutation appears to primarily alter the stereociliary bundle structure of IHCs followed by a change in ribbon size and exocytosis (Fig. 13).

The VGLUT3^{A224V/A224V} mouse as a model of progressive auditory neuropathy

Only a few mutations that cause a progressive and early-onset form of human deafness DFNA25 have been described (Ruel *et al.* 2008; Ryu *et al.* 2016). Among them, the c.616dupA variant of *SLC17A8* introduces a stop codon and hence leads to a truncated protein (Ryu *et al.* 2016; Qi *et al.* 2021). The p.A211V allele of *SLC17A8* is an additional variant that has not yet been fully characterized (Ruel *et al.* 2008). Here, the mouse line carrying two copies of the VGLUT3-p.A224V allele shows increasing threshold shift with age. Thus, this result further validates the p.A211V as one of the mutations responsible of DFNA25 (Ruel *et al.* 2008). However, the mild hearing impairment in the VGLUT3^{+/A224V} heterozygotes contrasts with the dominant transmission in DFNA25 (Greene *et al.* 2001; Thirlwall *et al.* 2003). This might be explained by the slow rate in the stereocilia alteration with respect to the short mouse lifespan. Decent DPOAEs were recorded in the knock-in mutant mouse. In contrast, otoacoustic emissions were absent in patients harbouring the p.A211V allele (Thirlwall *et al.* 2003). Thus, DFNA25 is more likely to be a progressive hearing loss in human rather than an auditory neuropathy (i.e. absent or desynchronized ABR with intact DPOAEs). Recent work has shown that VGLUT3 is expressed in OHCs to signal to the type II auditory nerve fibres (Weisz *et al.* 2021). However, robust DPOAEs measured in the VGLUT3-null mice do not support a role of VGLUT3 in cochlear amplification (Ruel *et al.* 2008; Seal *et al.* 2008; Kim *et al.* 2019). The lack of otoacoustic emissions in DFNA25 patients might be due to additional factors encountered during lifetime such as noise (Thirlwall *et al.* 2003). Consistently, the vulnerability to noise in mice carrying one or two variant alleles must be probed to determine whether acoustic injury accounts for the above discrepancies. Altogether, the mouse model harbouring the VGLUT3-p.A224V variant mimics a progressive hearing loss with auditory neuropathy features, but might be arguable so far as to consider it as a faithful model of DFNA25.

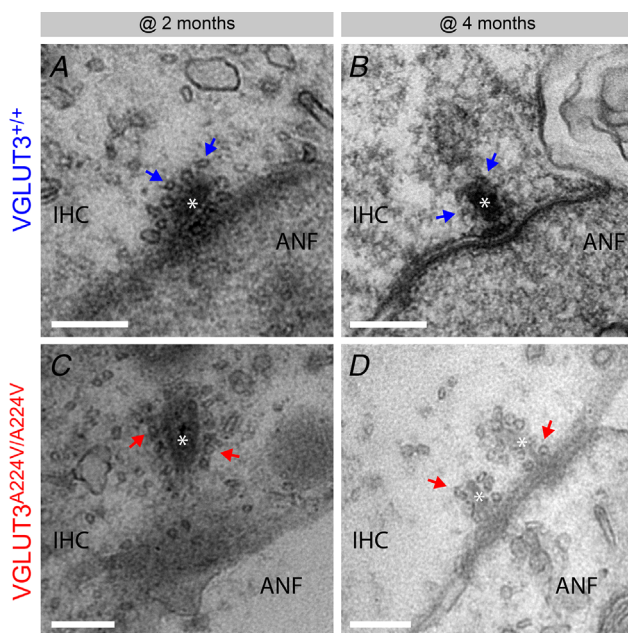


Figure 8. Transmission electron microscopy of synaptic ribbons in inner hair cells

A–D show examples of synaptic ribbons (white stars) surrounded by a halo of synaptic vesicles (arrows) in inner hair cells from VGLUT3^{+/+} (A and B) and VGLUT3^{A224V/A224V} (C and D) at 2 months (A, C) and 4 months (B, D). ANF: auditory nerve fibre. Scale bars: 200 nm.

Collapse of the stereocilia bundle in VGLUT3^{A224V/A224V}

In the VGLUT3^{A224V/A224V} homozygous mice, the major alteration lies in the stereocilia architecture from IHCs. This is somehow surprising since VGLUT3 is absent from IHC stereocilia and the loss of VGLUT3 does not

affect the transducer activity, as shown by intact hair cell receptor potential in the absence of VGLUT3 (Obholzer *et al.* 2008; Ruel *et al.* 2008). The p.A224V variant may result in a protein misfolding that leads to its aberrant aggregation and to distal adverse effects. A massive protein accumulation could create a traffic jam at the upper

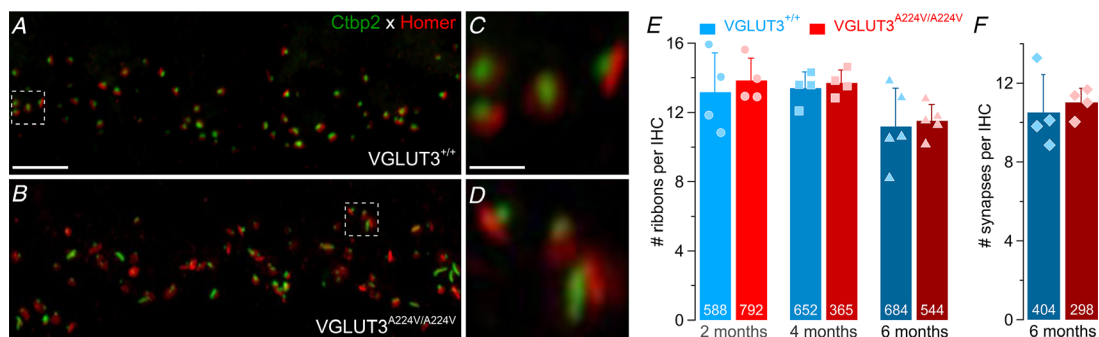


Figure 9. Ribbons and synapses count in inner hair cells

A–D, synaptic ribbons and post-synaptic densities immunostained with antibodies against Ctb2 (green) and Homer (red), respectively, in inner hair cells (IHCs) from 6 months VGLUT3^{+/+} (A, C) and VGLUT3^{A224V/A224V} (B, D) mice. Scale bar in (A and B): 5 μ m. C and D show high magnification of the white dashed squares from (A) and (B), respectively. Scale bar in (C, D): 1 μ m. E, mean \pm SD number of ribbons per IHC given by the immunostaining of Ctb2 from 2-, 4- and 6-month-old VGLUT3^{+/+} and VGLUT3^{A224V/A224V} mice. F, mean \pm SD number of synapses per IHC given by the juxtaposed immunostaining of Ctb2 and Homer from IHCs of 6-month-old VGLUT3^{+/+} and VGLUT3^{A224V/A224V} mice. White numbers indicate the number of IHCs analysed. Symbols represent average for individual cochleae. For each age and genotype, four cochleae have been used except for 6-month quantification in E (n = five cochleae).

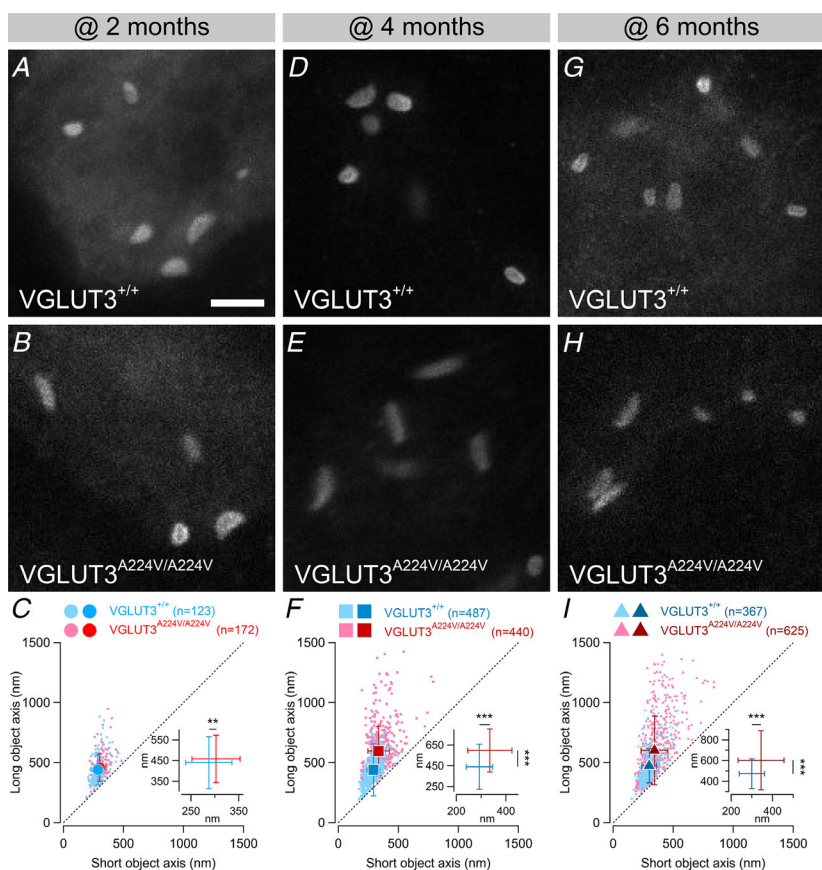


Figure 10. Synaptic ribbon morphology in inner hair cells

A–B, D–E and G–H, representative STED images of fluorescently labelled synaptic ribbons of 2-month (A, B), 4-month (D, E) and 6-month-old (G, H) inner hair cells from VGLUT3^{+/+} (A, D and G) and VGLUT3^{A224V/A224V} (B, E and H) mice. Scale bar: 1 μ m. C, F and I, long vs. short axes for VGLUT3^{+/+} (blue) and VGLUT3^{A224V/A224V} (red) ribbons at 2 months (C), 4 months (F) and 6 months (I). n indicates the number of ribbons examined, displayed as small dots. Insets show the mean values and SD for long vs. short axes. ** $P < 0.01$ and *** $P < 0.001$, Student's test for independent samples.

side of the nucleus and destabilize the route for protein turnover towards the stereocilia machinery. The failure in proteolysis has been shown to eventually provoke a disorientated stereocilia bundle (Freeman *et al.* 2019). In the human auditory neuropathy AUNA1, the over-expression of the diap3 protein leads to microtubule accumulation within the cuticular plate followed by the collapse of the stereocilia (Surel *et al.* 2016). However, in the striatum and hippocampal neurons, the point mutation leads to a reduced expression in the neuron terminals leaving the amount of VGLUT3 in the soma unaltered (Ramet *et al.* 2017). This argues against an abnormal accumulation of the p.A224V variant in the soma compartment preventing its distribution towards the terminals. In addition, in a virtual 3D model, replacing alanine in position 211 (224 in mouse) by a valine does not substantially modify the VGLUT3 structure as alanine and valine amino acid are closely related (Ramet *et al.* 2017). Finally, we did not observe an increase in the VGLUT3 immunofluorescence at the apical side of IHCs, although this relies on a semi-quantitative approach. The mechanisms underlying the homogeneous distribution of mutated VGLUT3 in hair cells *vs.* the differential expression in the central nervous system neurons are not known but hair cell can be assimilated to a single compartment without 'neurites'. Further experiments are therefore required to determine whether unfolded protein response operates in VGLUT3^{A224V/A224V} homozygous mice and whether the cytoskeleton is disrupted at the IHC apical side. Other mechanisms may contribute to the progressive destruction of the stereocilia. For instance, the genetic background of the mouse line used in our study is known to be homozygous for the defective

Cdh23ahl allele of the gene encoding cadherin 23, which is a constituent of hair cell stereocilia (Noben-Trauth *et al.* 2003; Siemens *et al.* 2004; Kazmierczak *et al.* 2007). Although VGLUT3 is not localized at the stereocilia bundle level, we cannot exclude the possibility that the Cdh23ahl allele potentiates, in any way, the stereocilia distortion. Large calcium influx in the C57Bl/6J has also been proposed to contribute to high-frequency hearing loss (Liu *et al.* 2019). Calcium overflow may exacerbate the phenotype in the VGLUT3^{A224V/A224V} mice but sound encoding is not altered at 3–4 months of age in the triple knock-out mice for endogenous intracellular calcium buffers, making a potential calcium overload that would deteriorate the hair cells unlikely (Pangršič *et al.* 2015).

Synaptic plasticity in VGLUT3^{A224V/A224V} mice

Akin to VGLUT3^{-/-} mice (Seal *et al.* 2008; Akil *et al.* 2012; Kim *et al.* 2019), we observe that the anatomy of synaptic ribbons changed at later stages. It has been shown that the synaptic ribbon size varies with the calcium influx amplitude (Martinez-Dunst *et al.* 1997; Schnee *et al.* 2005; Frank *et al.* 2009; Regus-Leidig & Specht, 2010; Sheets *et al.* 2012; Ohn *et al.* 2016). However, the lack of change in the calcium current amplitude in the IHCs of VGLUT3^{A224V/A224V} mice excludes such a mechanism. The p.A224V mutation occurs within a cytoplasmic loop that faces the pore of the transporter and thus may impede the loading of intra-vesicular glutamate. In this model, less glutamate could be released into the synaptic cleft leading to a reduced activity of the post-synaptic receptors and to poor recruitment of the

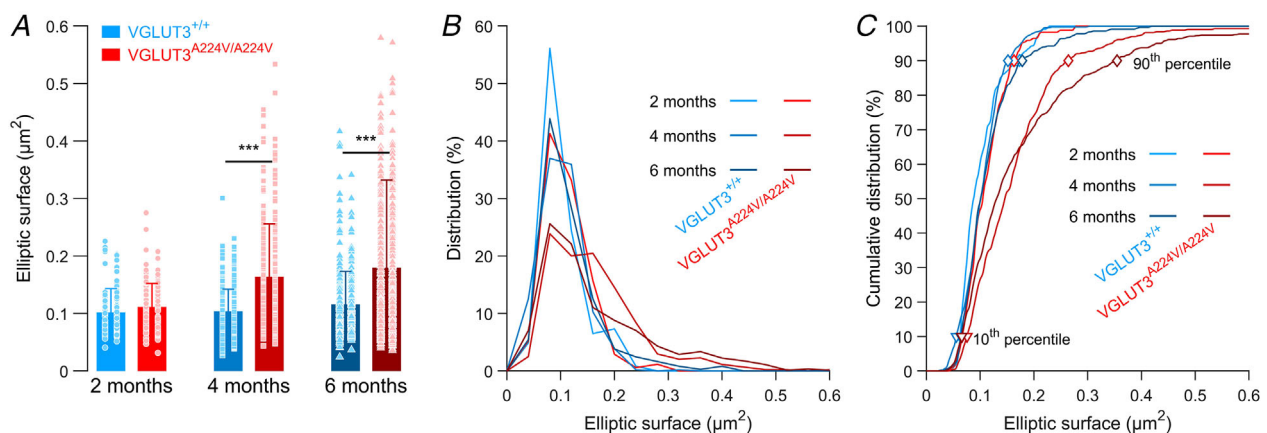


Figure 11. Increase of the elliptic surface of ribbon's section in inner hair cells

A, mean ± SD elliptic surface calculated from the ribbon's long and short axes lengths of 2-, 4- and 6-month-old IHCs from VGLUT3^{+/+} and VGLUT3^{A224V/A224V} mice. Symbols represent individual ribbons. B, distribution of the ribbons plots against the elliptical surface estimates of their cross-section derived from STED-imaging (bin width = 0.04 μm²). C, cumulative distribution of the ribbons as a function of the elliptical surface (bin width = 0.0001 μm²). Open symbols indicate the 10th (triangle) and 90th (diamond) percentile. Level of significance: *** $P < 0.001$, Student's test for independent samples.

afferent auditory nerve fibres. In hair cells, synapses with larger ribbons are associated with reduced activity (Merchan-Perez & Liberman, 1996; Sheets *et al.* 2012; Ohn *et al.* 2016; Kim *et al.* 2019). While high-spontaneous rate fibres with low-threshold activation project onto small synaptic ribbons on the pillar side, low-spontaneous rate (LSR) fibres with high-threshold activation connect to large ribbons on the modiolar side (Merchan-Perez &

Liberman, 1996; Liberman *et al.* 2011; Ohn *et al.* 2016). The increase in the number of thin and elongated synaptic ribbons may reflect an increase in the LSR fibre pool connecting the IHCs in VGLUT3^{A224V/A224V} mice. In this case, the hearing loss at late stages in VGLUT3^{A224V/A224V} mice could not only be attributable to the stereociliary bundle defect but also to the delayed and high jitter of the first-spike latency within auditory nerve fibres

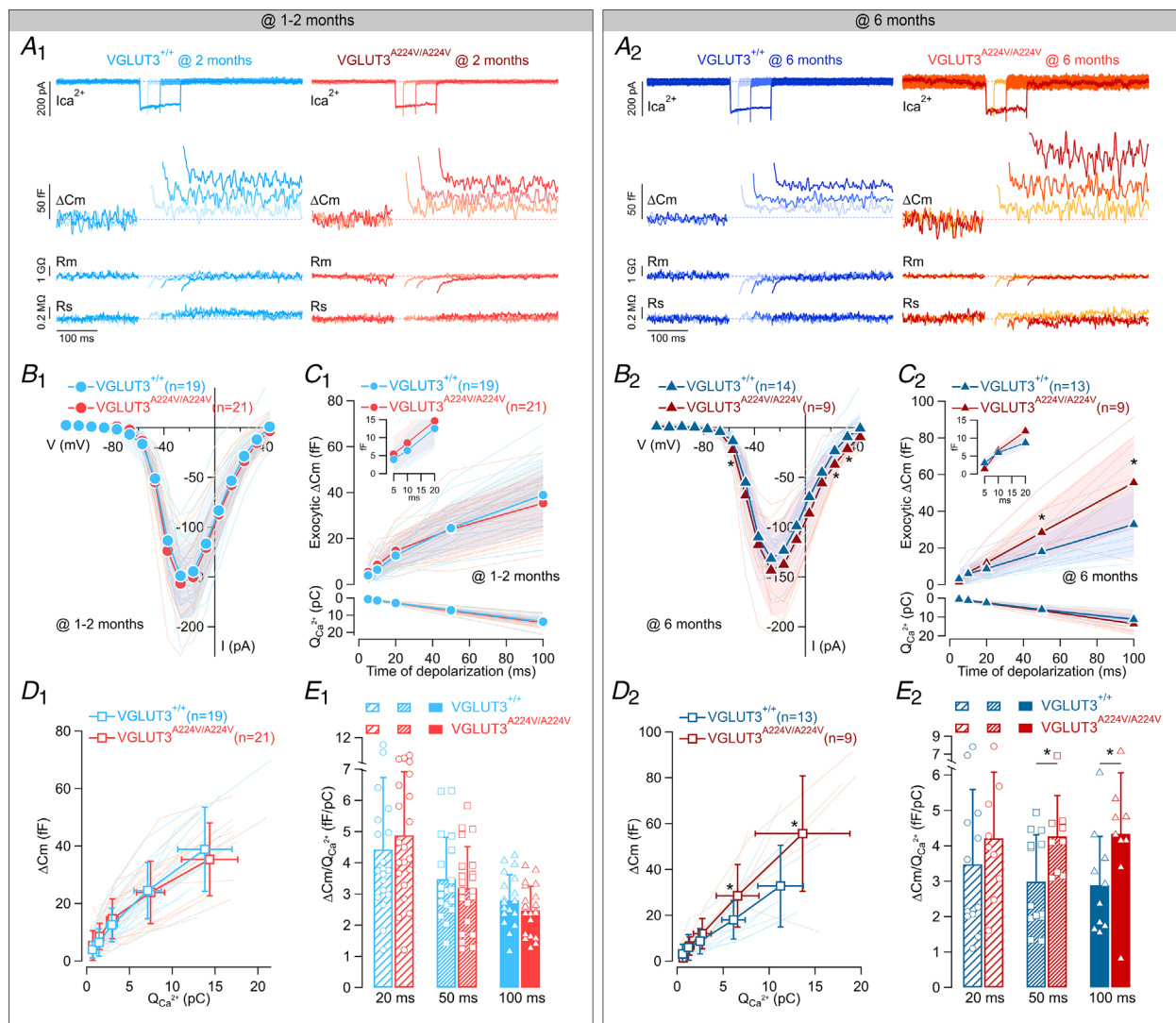


Figure 12. Increase of the sustained releasable pool exocytosis in 6-month-old inner hair cells of VGLUT3^{A224V/A224V} mice

A₁, E₂, perforated patch-clamp recordings of calcium-triggered exocytosis in 1/2- (A₁, E₁) and 6-month-old (A₂, E₂) inner hair cells (IHCs) of VGLUT3^{+/+} (blue) and VGLUT3^{A224V/A224V} mice (red). A₁, A₂, inward calcium current (I_{Ca}²⁺), membrane capacitance jump (ΔCm), membrane resistance (Rm) and series resistance (Rs) evoked by 20, 50 and 200 ms long depolarizing voltage steps from holding potential of -87 mV to -27 mV. B₁, B₂, Ca²⁺ current I/V relationships of IHCs from VGLUT3^{+/+} and VGLUT3^{A224V/A224V} mice. C₁, C₂, exocytic ΔCm and calcium charge Q_{Ca}²⁺ plotted against the duration of depolarization. Insets show the membrane capacitance increases in response to depolarizing voltage steps from 5 to 20 ms duration. Calcium-triggered exocytosis was evoked by depolarizations to -27 mV from holding potential of -87 mV. n: number of IHCs. D₁, D₂, exocytic ΔCm plotted against the corresponding calcium charge Q_{Ca}²⁺. E₁, E₂, release efficiency, ΔCm over calcium charge Q_{Ca}²⁺, for 20, 50 and 100 ms step depolarization. * P < 0.05, two-tailed Mann–Whitney Wilcoxon's test. Data are means ± SD. Thin lines and symbols represent individual cells.

(Bourien *et al.* 2014). Although we cannot rule out a reduction in the amount of glutamate released by the hair cells, the overexpression of VGLUT3-p.A224V variant in autaptic culture almost totally rescues the defect in exocytosis (Ramet *et al.* 2017). Consistently, the p.A224V mutation does not alter the vesicular uptake probed in heterologous system (Ramet *et al.* 2017). Thus, measurement of the afferent terminal activity is required to determine whether the p.A224V reduced the quantal size specifically at the hair cell ribbon synapse (Glowatzki & Fuchs, 2002; Özçete & Moser, 2020).

The IHCs calcium-triggered exocytosis probed by short-time duration corresponds to the RRP of synaptic vesicle. In our experiments, the RRP is not affected in IHCs from VGLUT3^{A224V/A224V} mice. In hair cells, calcium channels are densely packed underneath the pre-synaptic element and the RRP correlates to the membrane-proximal synaptic vesicles, that is, the vesicles tether to the synaptic body and docked to the plasma membrane (Khimich *et al.* 2005; Schnee *et al.* 2005; Rutherford & Roberts, 2006; Meyer *et al.* 2009; Frank *et al.* 2010; Pangršič *et al.* 2010; Graydon *et al.* 2011; Wong *et al.* 2014; Neef *et al.* 2018). Thus, the calcium current and the RRP size are likely to scale with the number of synapses (Meyer *et al.* 2009). The comparable calcium-current amplitude and similar amount of RRP between both genotypes are quite consistent with the preserved number of synapses.

The secretion evoked by longer time duration corresponds to the SRP of synaptic vesicles, which reflects the resupply of synaptic vesicles towards the release sites and/or fusion of remote vesicles with respect to the calcium channels (Moser & Beutner, 2000; Pangršič *et al.*

2010; Schnee *et al.* 2011; Moser *et al.* 2019). The secretion associated with the SRP is dramatically increased in mutant mice. This change may be due to a larger number of synaptic vesicles populating the synaptic ribbons as they become elongated in the mutant mouse (Kantardzhieva *et al.* 2013; Payne *et al.* 2021). In this hypothesis, the synaptic vesicles attached to the ribbon and facing the cytoplasm, the 'ribbon-associated SV' might be the morphological correlate to the SRP (Hull *et al.* 2006; Frank *et al.* 2010; Snellman *et al.* 2011; Maxeiner *et al.* 2016). However, the mutant models in which the ribbons are missing do not support this hypothesis: the ablation of RIBEYE in mouse or zebrafish hair cells leading to a ribbon-free active zone does not impair the secretion probed by capacitance measurements (Lv *et al.* 2016; Becker *et al.* 2018; Jean *et al.* 2018). In the triple knock-out mice for endogenous calcium buffers, a larger SRP has been measured using membrane capacitance patch-clamp recordings but the auditory thresholds and driven-rate of afferent fibres remained largely unaffected, suggesting extra-synaptic release (Pangršič *et al.* 2015). The increase in the SRP in the p.A224V homozygous mutant may be similar and reflect a form of pre-synaptic homeostatic plasticity, that is, release more glutamate to overcome a deficit in mechano-transduction with eventually a spiking rate reduction in the afferent auditory nerve fibre (Delvendahl *et al.* 2019).

In conclusion, these results highlight the critical role of VGLUT3 in maintaining the hair cell integrity to operate sound coding. The VGLUT3^{A224V/A224V} mouse will be a valuable asset to fully elucidate molecular mechanisms underlying DFNA25 and to identify an effective treatment.

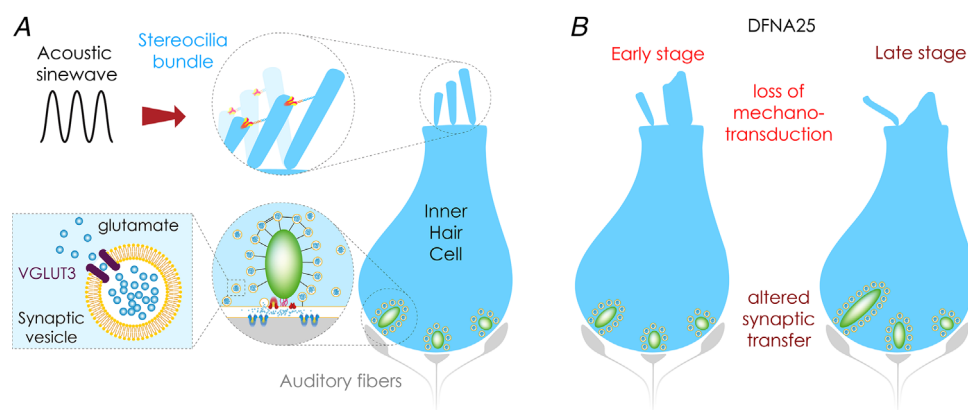


Figure 13. Hypothetical mechanisms underlying DFNA25

A, in response to incoming sound stimulation, stereocilia are deflected, leading to the mechanotransducer channel opening and the depolarization of the inner hair cell. The calcium influx through the voltage-gated calcium channel triggers the exocytosis of glutamate-laden synaptic vesicles. The release of glutamate in the synaptic cleft activates the auditory nerve fibre, which conveys the neural message to the brainstem. B, in the VGLUT3^{A224V/A224V} mice, the collapse of the stereocilia impairs the mechanotransduction, degrading the hair cell receptor potential and most probably reducing the activity within the auditory nerve fibres. C, at later stage, the synaptic ribbons undergo a morphological change that may additionally downgrade the sound-stimulation encoding.

References

- Akil O, Seal RP, Burke K, Wang C, Alemi A, During M, Edwards RH & Lustig LR (2012). Restoration of hearing in the VGLUT3 knockout mouse using virally mediated gene therapy. *Neuron* **75**, 283–293.
- Becker L, Schnee ME, Niwa M, Sun W, Maxeiner S, Talaei S, Kachar B, Rutherford MA & Ricci AJ (2018). The pre-synaptic ribbon maintains vesicle populations at the hair cell afferent fiber synapse. *eLife* **7**, e30241.
- Bourien J, Tang Y, Batrel C, Huet A, Lenoir M, Ladrech S, Desmadryl G, Nouvian R, Puel J-L & Wang J (2014). Contribution of auditory nerve fibers to compound action potential of the auditory nerve. *J Neurophysiol* **112**, 1025–1039.
- Delvendahl I, Kita K & Müller M (2019). Rapid and sustained homeostatic control of presynaptic exocytosis at a central synapse. *Proc Natl Acad Sci USA* **116**, 23783–23789.
- El Mestikawy S, Wallén-Mackenzie Å, Fortin GM, Descarries L & Trudeau L-E (2011). From glutamate co-release to vesicular synergy: vesicular glutamate transporters. *Nat Rev Neurosci* **12**, 204–216.
- Frank T, Khimich D, Neef A & Moser T (2009). Mechanisms contributing to synaptic Ca^{2+} signals and their heterogeneity in hair cells. *Proc Natl Acad Sci U S A* **106**, 4483–4488.
- Frank T, Rutherford MA, Strenzke N, Neef A, Pangršič T, Khimich D, Fejtova A, Gundelfinger ED, Liberman MC, Harke B, Bryan KE, Lee A, Egner A, Riedel D, Moser T (2010). Bassoon and the Synaptic Ribbon Organize Ca^{2+} Channels and Vesicles to Add Release Sites and Promote Refilling. *Neuron*, **68**, (4), 724. –738.
- Freeman S, Mateo Sánchez S, Pouyo R, Van Lerberghe P-B, Hanon K, Thelen N, Thiry M, Morelli G, Van Hees L, Laguesse S, Chariot A, Nguyen L, Delacroix L & Malgrange B (2019). Proteostasis is essential during cochlear development for neuron survival and hair cell polarity. *EMBO Rep* **20**, e47097.
- Freneau RT, Burman J, Qureshi T, Tran CH, Proctor J, Johnson J, Zhang H, Sulzer D, Copenhagen DR, Storm-Mathisen J, Reimer RJ, Chaudhry FA & Edwards RH (2002). The identification of vesicular glutamate transporter 3 suggests novel modes of signaling by glutamate. *Proc Natl Acad Sci U S A* **99**, 14488–14493.
- Glowatzki E & Fuchs PA (2002). Transmitter release at the hair cell ribbon synapse. *Nat Neurosci* **5**, 147–154.
- Gras C, Herzog E, Bellenchi GC, Bernard V, Ravassard P, Pohl M, Gasnier B, Giros B & El Mestikawy S (2002). A third vesicular glutamate transporter expressed by cholinergic and serotonergic neurons. *J Neurosci* **22**, 5442–5451.
- Graydon CW, Cho S, Li G-L, Kachar B & von Gersdorff H (2011). Sharp Ca^{2+} nanodomains beneath the ribbon promote highly synchronous multivesicular release at hair cell synapses. *J Neurosci* **31**, 16637–16650.
- Greene CC, McMillan PM, Barker SE, Kurnool P, Lomax MI, Burmeister M & Lesperance MM (2001). DFNA25, a novel locus for dominant nonsyndromic hereditary hearing impairment, maps to 12q21-24. *Am J Hum Genet* **68**, 254–260.
- Grundy D (2015). Principles and standards for reporting animal experiments in *The Journal of Physiology* and *Experimental Physiology*. *J Physiol* **593**, 2547–2549.
- Hull C, Studholme K, Yazulla S & von Gersdorff H (2006). Diurnal changes in exocytosis and the number of synaptic ribbons at active zones of an ON-type bipolar cell terminal. *J Neurophysiol* **96**, 2025–2033.
- Jean P, Lopez de la Morena D, Michanski S, Jaime Tobón LM, Chakrabarti R, Picher MM, Neef J, Jung S, Gültas M, Maxeiner S, Neef A, Wichmann C, Strenzke N, Grabner C & Moser T (2018). The synaptic ribbon is critical for sound encoding at high rates and with temporal precision. *eLife* **7**, e29275.
- Kantardzhieva A, Liberman MC & Sewell WF (2013). Quantitative analysis of ribbons, vesicles, and cisterns at the cat inner hair cell synapse: correlations with spontaneous rate. *J Comp Neurol* **521**, 3260–3271.
- Kazmierczak P, Sakaguchi H, Tokita J, Wilson-Kubalek EM, Milligan RA, Müller U & Kachar B (2007). Cadherin 23 and protocadherin 15 interact to form tip-link filaments in sensory hair cells. *Nature* **449**, 87–91.
- Khimich D, Nouvian R, Pujol R, tom Dieck S, Egner A, Gundelfinger ED & Moser T (2005). Hair cell synaptic ribbons are essential for synchronous auditory signalling. *Nature* **434**, 889–894.
- Kim KX, Payne S, Yang-Hood A, Li S-Z, Davis B, Carlquist J, V-Ghaffari B, Gantz JA, Kallogjeri D, Fitzpatrick JAJ, Ohlemiller KK, Hirose K & Rutherford MA (2019). Vesicular glutamatergic transmission in noise-induced loss and repair of cochlear ribbon synapses. *J Neurosci* **39**, 4434–4447.
- Liberman LD, Wang H & Liberman MC (2011). Opposing gradients of ribbon size and ampa receptor expression underlie sensitivity differences among cochlear-nerve/hair-cell synapses. *J Neurosci* **31**, 801–808.
- Lindau M, Neher E (1988) Patch-clamp techniques for time-resolved capacitance measurements in single cells. *Pflügers Archiv European Journal of Physiology*, **411**, 137–146.
- Liu H, Li G, Lu J, Gao Y-G, Song L, Li G-L & Wu H (2019). Cellular differences in the cochlea of CBA and B6 mice may underlie their difference in susceptibility to hearing loss. *Front Cell Neurosci* **13**, 60.
- Lv C, Stewart WJ, Akanyeti O, Frederick C, Zhu J, Santos-Sacchi J, Sheets L, Liao JC & Zenisek D (2016). Synaptic ribbons require ribeye for electron density, proper synaptic localization, and recruitment of calcium channels. *Cell Rep* **15**, 2784–2795.
- Martinez-Dunst C, Michaels RL & Fuchs PA (1997). Release sites and calcium channels in hair cells of the chick's cochlea. *J Neurosci* **17**, 9133–9144.
- Maxeiner S, Luo F, Tan A, Schmitz F & Südhof TC (2016). How to make a synaptic ribbon: RIBEYE deletion abolishes ribbons in retinal synapses and disrupts neurotransmitter release. *EMBO J* **35**, 1098–1114.
- Merchan-Perez A & Liberman MC (1996). Ultrastructural differences among afferent synapses on cochlear hair cells: correlations with spontaneous discharge rate. *J Comp Neurol* **371**, 208–221.

- Meyer AC, Frank T, Khimich D, Hoch G, Riedel D, Chapochnikov NM, Yarin YM, Harke B, Hell SW, Egner A & Moser T (2009). Tuning of synapse number, structure and function in the cochlea. *Nat Neurosci* **12**, 444–453.
- Michanski S, Smaluch K, Steyer AM, Chakrabarti R, Setz C, Oestreicher D, Fischer C, Möbius W, Moser T, Vogl C & Wichmann C (2019). Mapping developmental maturation of inner hair cell ribbon synapses in the apical mouse cochlea. *Proc Natl Acad Sci USA* **116**, 6415–6424.
- Moser T & Beutner D (2000). Kinetics of exocytosis and endocytosis at the cochlear inner hair cell afferent synapse of the mouse. *Proc Natl Acad Sci U S A* **97**, 883–888.
- Moser T, Grabner CP & Schmitz F (2019). Sensory processing at ribbon synapses in the retina and the cochlea. *Physiol Rev* **100**, 103–144.
- Neef J, Urban NT, Ohn T-L, Frank T, Jean P, Hell SW, Willig KI & Moser T (2018). Quantitative optical nanophysiology of Ca^{2+} signaling at inner hair cell active zones. *Nat Commun* **9**, 290.
- Noben-Trauth K, Zheng QY & Johnson KR (2003). Association of cadherin 23 with polygenic inheritance and genetic modification of sensorineural hearing loss. *Nat Genet* **35**, 21–23.
- Obholzer N, Wolfson S, Trapani JG, Mo W, Nechiporuk A, Busch-Nentwich E, Seiler C, Sidi S, Sollner C, Duncan RN, Boehland A & Nicolson T (2008). Vesicular glutamate transporter 3 is required for synaptic transmission in zebrafish hair cells. *J Neurosci* **28**, 2110–2118.
- Ohn T-L, Rutherford MA, Jing Z, Jung S, Duque-Afonso CJ, Hoch G, Picher MM, Scharinger A, Strenzke N & Moser T (2016). Hair cells use active zones with different voltage dependence of Ca^{2+} influx to decompose sounds into complementary neural codes. *Proc Natl Acad Sci U S A* **113**, E4716–E4725.
- Özçete Özge D, Moser Tobias (2021) A sensory cell diversifies its output by varying Ca^{2+} influx-release coupling among active zones. *The EMBO Journal*, **40**, (5), <http://doi.org/10.15252/embj.2020106010>
- Pangršič T, Gabrielaitis M, Michanski S, Schwaller B, Wolf F, Strenzke N & Moser T (2015). EF-hand protein Ca^{2+} buffers regulate Ca^{2+} influx and exocytosis in sensory hair cells. *Proc Natl Acad Sci U S A* **112**, E1028–E1037.
- Pangršič T, Lasarow L, Reuter K, Takago H, Schwander M, Riedel D, Frank T, Tarantino LM, Bailey JS, Strenzke N, Brose N, Müller U, Reisinger E & Moser T (2010). Hearing requires otoferlin-dependent efficient replenishment of synaptic vesicles in hair cells. *Nat Neurosci* **13**, 869–876.
- Payne SA, Joens MS, Chung H, Skigen N, Frank A, Gattani S, Vaughn K, Schwed A, Nester M, Bhattacharyya A, Iyer G, Davis B, Carlquist J, Patel H, Fitzpatrick JAJ & Rutherford MA (2021). Maturation of heterogeneity in afferent synapse ultrastructure in the mouse cochlea. *Front Synaptic Neurosci* **13**, 678575.
- Qi Y, Gong S, Liu K & Song Y (2021). The c.824C>A and c.616dupA mutations in the SLC17a8 gene are associated with auditory neuropathy and lead to defective expression of VGLUT3. *NeuroReport* **32**, 949–956.
- Ramet L, Zimmermann J, Bersot T, Poirel O, De Gois S, Silm K, Sakae DY, Mansouri-Guilani N, Bourque M-J, Trudeau L-E, Pietrancosta N, Dumas S, Bernard V, Rosenmund C & El Mestikawy S (2017). Characterization of a human point mutation of VGLUT3 (p.A211V) in the rodent brain suggests a nonuniform distribution of the transporter in synaptic vesicles. *J Neurosci* **37**, 4181–4199.
- Regus-Leidig H & Specht D (2010). Stability of active zone components at the photoreceptor ribbon complex. *Mol Vis* **16**, 2690–2700.
- Ruel J, Emery S, Nouvian R, Bersot T, Amilhon B, Van Rybroek JM, Rebillard G, Lenoir M, Eybalin M, Delprat B, Sivakumaran TA, Giros B, El Mestikawy S, Moser T, Smith RJH, Lesperance MM & Puel J-L (2008). Impairment of SLC17A8 encoding vesicular glutamate transporter-3, vglut3, underlies nonsyndromic deafness DFNA25 and inner hair cell dysfunction in null mice. *Am J Hum Genet* **83**, 278–292.
- Rutherford MA & Roberts WM (2006). Frequency selectivity of synaptic exocytosis in frog saccular hair cells. *Proc Natl Acad Sci U S A* **103**, 2898–2903.
- Ryu N, Sagong B, Park H-J, Kim M-A, Lee K-Y, Choi JY & Kim U-K (2016). Screening of the SLC17A8 gene as a causative factor for autosomal dominant non-syndromic hearing loss in Koreans. *BMC Med Genet* **17**, 6.
- Schnee ME, Lawton DM, Furness DN, Benke TA & Ricci AJ (2005). Auditory hair cell-afferent fiber synapses are specialized to operate at their best frequencies. *Neuron* **47**, 243–254.
- Schnee ME, Santos-Sacchi J, Castellano-Muñoz M, Kong J-H & Ricci AJ (2011). Calcium-dependent synaptic vesicle trafficking underlies indefatigable release at the hair cell afferent fiber synapse. *Neuron* **70**, 326–338.
- Seal RP, Akil O, Yi E, Weber CM, Grant L, Yoo J, Clause A, Kandler K, Noebels JL, Glowatzki E, Lustig LR & Edwards RH (2008). Sensorineural deafness and seizures in mice lacking vesicular glutamate transporter 3. *Neuron* **57**, 263–275.
- Sheets L, Kindt KS & Nicolson T (2012). Presynaptic $\text{CaV}1.3$ channels regulate synaptic ribbon size and are required for synaptic maintenance in sensory hair cells. *J Neurosci* **32**, 17273–17286.
- Siemens J, Lillo C, Dumont RA, Reynolds A, Williams DS, Gillespie PG & Müller U (2004). Cadherin 23 is a component of the tip link in hair-cell stereocilia. *Nature* **428**, 950–955.
- Snellman J, Mehta B, Babai N, Bartoletti TM, Akmentin W, Francis A, Matthews G, Thoreson W & Zenisek D (2011). Acute destruction of the synaptic ribbon reveals a role for the ribbon in vesicle priming. *Nat Neurosci* **14**, 1135–1141.
- Surel C, Guillet M, Lenoir M, Bourien J, Sendin G, Joly W, Delprat B, Lesperance MM, Puel J-L & Nouvian R (2016). Remodeling of the inner hair cell microtubule meshwork in a mouse model of auditory neuropathy AUNA1. *eNeuro* **3**, ENEURO.0295-16.2016.
- Takamori S, Malherbe P, Broger C & Jahn R (2002). Molecular cloning and functional characterization of human vesicular glutamate transporter 3. *EMBO Rep* **3**, 798–803.

Thirlwall AS, Brown DJ, McMillan PM, Barker SE & Lesperance MM (2003). Phenotypic characterization of hereditary hearing impairment linked to DFNA25. *Arch Otolaryngol Head Neck Surg* **129**, 830–835.

Weisz CJC, Williams S-PG, Eckard CS, Divito CB, Ferreira DW, Fantetti KN, Dettwyler SA, Cai H-M, Rubio ME, Kandler K & Seal RP (2021). Outer hair cell glutamate signaling through type II spiral ganglion afferents activates neurons in the cochlear nucleus in response to non-damaging sounds. *J Neurosci* **41**, 2930–2943.

Wong AB, Rutherford MA, Gabrielaitis M, Pangršič T, Göttfert F, Frank T, Michanski S, Hell S, Wolf F, Wichmann C & Moser T (2014). Developmental refinement of hair cell synapses tightens the coupling of Ca^{2+} influx to exocytosis. *EMBO J* **33**, 247–264.

Zhang FX, Pang YW, Zhang MM, Zhang T, Dong YL, Lai CH, Shum DKY, Chan YS, Li JL & Li YQ (2011). Expression of vesicular glutamate transporters in peripheral vestibular structures and vestibular nuclear complex of rat. *Neuroscience* **173**, 179–189.

Additional information

Data availability statement

The data that support the findings of this study are available from the corresponding authors upon reasonable request.

Competing interests

All authors declare no competing interests.

Author contributions

Y.J., C.P.P., S.M., M.G., G.S., J.B., J.W., R.P., S.E.M., J.L.P. and R.N. designed research. Y.J., C.P.P., S.M., M.G., G.S., J.W., R.P.

performed research. J.B., S.E.M., J.L.P. and R.N. contributed unpublished reagents/analytic tools. Y.J., C.P.P., S.M., M.G., J.B. and R.N. analysed data. Y.J., C.P.P., J.B., J.W., S.E.M., J.L.P. and R.N. wrote the manuscript.

Acknowledgements

The authors thank Chantal Cazeville for her expertise and assistance in electron microscopy.

Funding

This work was supported by an EU Horizon 2020 Marie Skłodowska-Curie Action Innovative Training network, H2020-MSCA-ITN-2016 [LISTEN - 722098], by the Fondation de l'Avenir (Et2-675), Inserm Grant (U1051-Dot 02_2016) and the Fondation pour l'Audition (FPA RD-2016-2 and 2018-017I1). S.M. was supported by a fellowship from the 'Ecole de l'INSERM-Liliane Bettencourt'. G.S. is a recipient of the postdoctoral fellowship of the University of Montpellier.

Keywords

cochlea, deafness, exocytosis, sensory cells

Supporting information

Additional supporting information can be found online in the Supporting Information section at the end of the HTML view of the article. Supporting information files available:

Peer Review History

Statistical Summary Document

Supporting Information